

Two-Dimensional Materials for Energy-Efficient Spin-Orbit Torque Devices

Yuting Liu and Qiming Shao*

*Department of Electronic and Computer Engineering, Hong Kong University of Science
and Technology, Clear Water Bay, Kowloon, Hong Kong, China*

E-mail: eqshao@ust.hk

Abstract

Spin-orbit torques (SOTs), which rely on spin current generation from charge current in a nonmagnetic material, promise an energy-efficient scheme for manipulating magnetization in magnetic devices. A critical topic for spintronic devices using SOTs is to enhance the charge to spin conversion efficiency. Besides, the current-induced spin polarization is usually limited to in-plane, whereas out-of-plane spin polarization could be favored for efficient perpendicular magnetization switching. Recent advances in utilizing two important classes of two-dimensional materials—topological insulators and transition-metal dichalcogenides—as spin sources to generate SOT shed light on addressing these challenges. Topological insulators such as bismuth selenide have shown a giant SOT efficiency, which is larger than those from three-dimensional heavy metals by at least one order of magnitude. Transition-metal dichalcogenides such as tungsten telluride have shown a current-induced out-of-plane spin polarization, which is allowed by the reduced symmetry. In this review, we use symmetry arguments to predict and analyze SOTs in two-dimensional material-based heterostructures. We summarize the recent progress of SOT studies based on topological insulators and transition-metal dichalcogenides and show how these results are in line with the symmetry arguments.

At last, we identify unsolved issues in the current studies and suggest three potential research directions in this field.

Ubiquitous smart devices and the Internet of Things create tremendous data every day, shifting computing diagram towards data-driven. Computing and memory units in traditional computers are physically separate, which leads to huge energy cost and time delay. Emerging computer architectures bring computing and memory units together for data-intensive applications. Magneto-resistive random-access memory (MRAM) is the leading contender for future embedded nonvolatile memory due to its high speed, energy efficiency, and theoretically unlimited endurance.¹ MRAM and many other magnetic or spintronic devices rely on the efficient manipulation of magnetic moments through electrically generated spin current. Looking for efficient methods to generate spin current with the least possible charge current is an essential task for spintronics. Recently, in nonmagnetic materials with strong spin-orbit coupling, spin Hall effect or Rashba effect has been shown to generate a large spin current and thus a strong spin-orbit torque (SOT) on the adjacent ferromagnet (FM), enabling magnetic domain wall motion, magnetization switching, and magnetic resonance.²⁻⁵ As a result, SOT-based devices, such as SOT-MRAM, magnetic nonvolatile logic,⁶ and nano-oscillators⁷ have attracted widespread attention for ultralow-power nonvolatile memory and logic applications.

Commonly used SOT source materials are three-dimensional (3D) heavy metals (HM), such as Pt, Ta, and W, which face two challenges. *First*, in most cases, the damping-like SOT plays a dominant role in magnetization switching since it compensates the magnetic damping. The damping-like SOT efficiencies of HM range from 0.1 to 0.3.⁵ To reduce the switching energy, improved SOT efficiency is required. *Second*, in HM/FM heterostructures with perpendicular magnetic anisotropy (PMA), the damping-like SOT generated by HMs lies in the film plane as required by a global twofold rotational symmetry, which does not allow a deterministic and energy-efficient switching without an external magnetic field.⁸ For MRAM technology, perpendicularly magnetized magnets are preferred because they require

a much lower switching current compared with that of in-plane magnetized magnets. To achieve deterministic and energy-efficient switching of a magnet with PMA, the out-of-plane damping-like SOT is desired.

Recently, two important classes of two-dimensional (2D) materials emerged for generating SOTs, which allow one to address the above-mentioned two challenges. The first class is the 2D Bi_2Se_3 family, which are 3D topological insulators (TIs). TIs exhibit a giant damping-like SOT efficiency larger than 100 at low temperatures due to the spin momentum locking of topological surface states.⁹ The orders of magnitude of improvement of SOT efficiency can potentially bring a much lower switching current density for SOT devices. The second class is 2D transition-metal dichalcogenides (TMDs), some of which have a very strong spin-orbit coupling and much lower global symmetries than 3D HMs. For example, a low-symmetry 2D TMD, $\text{T}_d\text{-WTe}_2$ with an orthorhombic lattice structure allows for the generation of out-of-plane damping-like SOT,¹⁰ which could potentially enable deterministic and energy-efficient switching of the perpendicular magnet.

2D materials offer many exceptional properties for spintronic applications, including but not limited to electrical¹¹ and chemical¹² tunability of spintronic properties, intrinsic ferromagnetism^{13,14} and antiferromagnetism,¹⁴ long spin diffusion length,^{15,16} large and multidirectional spin-to-charge conversion efficiency,¹⁷ and large charge-to-spin conversion or SOT efficiency.^{9,18} In this review, we highlight two key advantages regarding SOTs. First, 2D materials are crystalline materials down to the monolayer limit and they have diverse band structures. Many 2D materials with a strong spin-orbit coupling show topological properties, which are appealing to generating large SOTs. For example, $\text{T}_d\text{-WTe}_2$ is Weyl semimetal in the bulk form¹⁹ and 2D TI in the monolayer limit.²⁰ Second, 2D materials have diverse symmetry properties, which could be used to guide researchers to identify unconventional SOTs, *i.e.*, SOTs with unconventional directions. For example, while an out-of-plane damping-like SOT cannot be generated by 2H-TMDs that have preserved twofold rotational symmetry, it can be generated by 1T'- or T_d -TMDs that have a broken twofold rotational symmetry.

Therefore, studying SOTs generated by 2D materials is of critical importance for spintronic applications.

Motivated by the breakthroughs in SOT generated by TIs and TMDs, intensive investigations of SOT devices based on 2D materials are ongoing. SOTs have been experimentally studied in heterostructures composed of an FM and a 2D material, including TIs (Bi_2Se_3 family,^{9,11,18}) semiconducting TMDs (2H-MoS₂^{21,22} and 2H-WSe₂,²²) metallic TMDs ($\text{T}_d\text{-WTe}_2$,^{10,23} 1T'-MoTe₂,²⁴ 1T'-TaTe₂,²⁵, PtTe₂²⁶) and superconducting TMD (NbSe₂²⁷). While the number of experimental reports about SOTs generated by 2D materials has dramatically increased, there is no systematic review of symmetry analysis and experimental results that could help identify the key open questions and guide further studies.

In this review, we first present the SOT prediction based on symmetry argument and show the theoretical predictions of SOTs generated by various 2D materials according to their symmetry properties. Then, we review recent experimental progress about SOT studies in 2D material-based heterostructures. We will focus on TI and TMD systems. Through this summary, we will identify how the symmetry analysis aligns with the experimental observation and what is missing in current studies. Besides, we review the current understanding of the origins of SOTs in these heterostructures and the progress of large-scale growth of high-quality 2D materials for spintronic applications. At last, we provide a conclusion and outlook that briefly summarizes the article and points out three potential research directions.

Background of Research

There are two important schemes for generating spin torques: spin-transfer torques (STTs) and SOTs. Here, we will use a comparison between these two schemes to show the significance of a large out-of-plane damping-like torque for switching perpendicular magnetization. STTs are originated from spins polarized by a magnetic material, which can be transferred to another magnetic material to exert a spin torque. The current-induced spin polarization

unit vector $\boldsymbol{\sigma}$ is collinear with the magnetization unit vector (\mathbf{m}) of the ferromagnetic fixed layer. STTs were first theoretically proposed by Slonczewski²⁸ and Berger²⁹ in 1996 and then later realized experimentally in 1999.^{30,31} There are two types of STTs: field-like (FL) or adiabatic STT and Slonczewski or non-adiabatic (anti-)damping-like (DL) STT. FL-STT and DL-STT are written as $\vec{\boldsymbol{\tau}}_{\text{FL}} = \tau_{\text{FL}} \mathbf{m} \times \boldsymbol{\sigma}$ and $\vec{\boldsymbol{\tau}}_{\text{DL}} = \tau_{\text{DL}} \mathbf{m} \times (\mathbf{m} \times \boldsymbol{\sigma})$, respectively, where τ_{FL} and τ_{DL} are the magnitude of FL-STT and DL-STT, respectively. In the equilibrium, \mathbf{m} 's of the fixed layer and the free layer are collinear (parallel or antiparallel), resulting in zero STTs. Thus, STT driven switching is normally initiated by thermal effects which limit STT switching time and minimum error rate.³²

SOTs mainly result from spin-orbit coupling (SOC) of a nonmagnetic material, which allows a charge current to be converted to a spin current and then exert a spin torque on the adjacent magnetic material. FL-SOT and DL-SOT have the same expressions as the FL-STT and DL-STT. However, the current-induced spin polarization $\boldsymbol{\sigma}$ in the SOT case is originated from the SOC and thus its direction is not necessarily collinear with the initial \mathbf{m} of the ferromagnetic free layer. While there were early theoretical studies about SOTs in 2008-2009^{33,34} and experimental demonstration of SOT-induced magnetization re-orientation in (Ga,Mn)As in 2009³⁵ potential and relevance of SOTs for real applications are brought to attention by room-temperature SOT-induced, magnetization switching in Pt/Co/AlO_x in 2011³ and Ta/CoFeB/MgO-based magnetic tunnel junctions (MTJs) in 2012.⁴

There are two important advantages of SOTs in comparison to STTs. First, for STT-MARM (see Fig. 1 (a)), the writing current needs to go through the MTJ, causing the easy breakdown of nanometer-thick MgO tunnel barrier in the MTJ. In contrast, for SOT-MRAM (Fig. 1 (b)), the writing current is passing through the metal line instead of MTJs, greatly improving the endurance of the SOT-MRAM. Second, STT efficiency (η) is fundamentally limited by the spin polarization at the Fermi level of ferromagnetic metal, which cannot be larger than one. However, recent advances have shown that SOT efficiency (ξ) can be larger than one in some topological materials, such as 3D topological insulators Bi₂Se₃¹⁸ and (BiSb)₂Te₃.⁹

A comprehensive introduction to STT- and SOT-MRAM can be found in Wang *et al.*^{6,36}

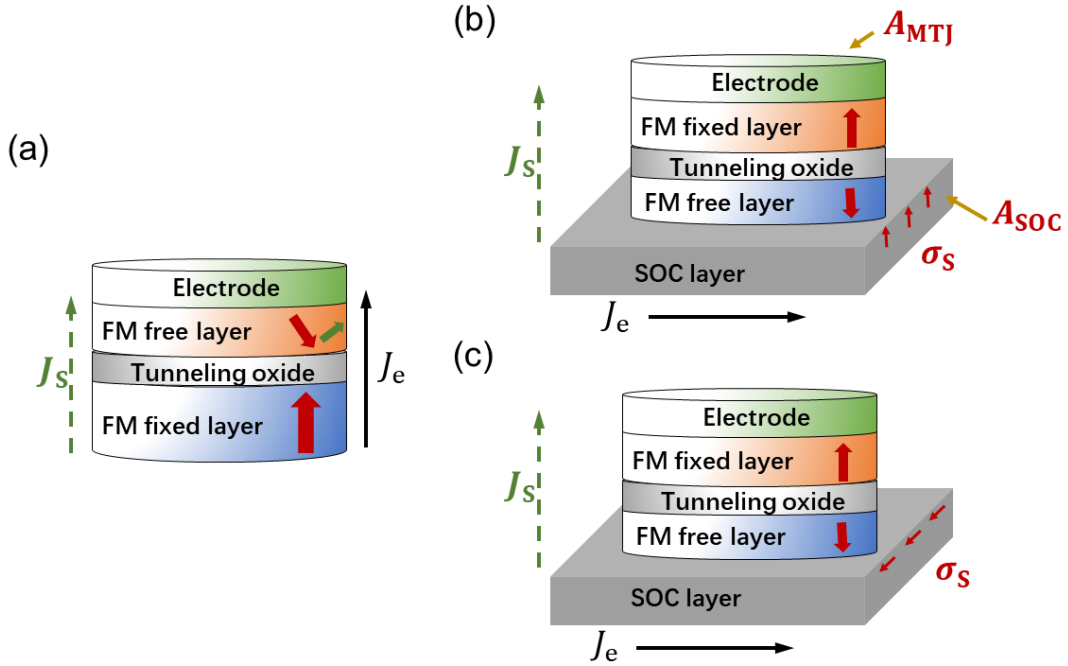


Figure 1: Schematics of MRAMs. (a) STT-MRAM unit cell, (b) and (c) SOT-MRAM unit cells with current-induced out-of-plane and in-plane spin polarization. Only the spin polarization near the top surface of the SOC layer has been shown in (b) and (c).

The comparison between critical currents of SOT- and STT-MRAM (I_{SOT} and I_{STT}) under the assumption of a single-domain magnet can be written as³⁶

$$\frac{I_{SOT}}{I_{STT}} \approx \frac{\eta A_{SOC}}{\xi A_{MTJ}}, \quad (1)$$

where A_{SOC} and A_{MTJ} are the cross-section area of the SOC layer and MTJ layer, respectively. As shown in Fig. 1 (b), the width of the SOC layer will be at the order of MTJ diameter and the thickness of the SOC layer is typically several nanometers, which is much smaller than typical MTJ diameter (tens to hundreds of nanometers). Therefore, $A_{SOC}/A_{MTJ} < 1$. From Eq. 1, if $\eta/\xi < 1$, we will have $I_{SOT}/I_{STT} < 1$. This suggests that the SOT-MRAM has a significant advantage regarding the writing current over the STT-MRAM if one can utilize a SOC layer with a large ξ . However, Eq. 1 has an assumption that is not valid in most of the

SOT experiments. The assumption is that the current-induced spin polarization is collinear with the initial magnetization of the free layer, which is always true for STT-MRAM but not for SOT-MRAM. To date, most of the thin film SOC materials, such as Pt, Ta, and W, can only generate a spin polarization lying in the film plane, which is orthogonal to the initial \mathbf{m} of a free layer with PMA as shown in Fig. 1 (c). Note that the ferromagnetic layers with PMA are preferred for MRAM due to a much better scalability and lower writing energy.³⁶ In these cases, the ratio of I_{SOT} to I_{STT} (single-domain magnet consumption) is given by^{10,37,38}

$$\frac{I_{\text{SOT}}}{I_{\text{STT}}} \approx \frac{\eta}{2\alpha\xi} \frac{A_{\text{SOC}}}{A_{\text{MTJ}}}, \quad (2)$$

where α is the Gilbert damping factor. Since α is typically on the order of 0.01, ξ needs to be orders of magnitude larger than η to achieve a smaller I_{SOT} compared with I_{STT} . So we need to figure out how to generate an out-of-plane spin polarization in SOT-MRAM to gain the energy advantage shown in Eq. 1. Moreover, the thermal incubation time is not needed for SOT switching when both the in-plane and out-of-plane spin polarizations exist. In the following, we will use symmetry arguments to understand why there is only an in-plane spin polarization in HM/FM heterostructures and how we can generate an out-of-plane spin polarization.

In a material or material heterostructure with a sizable SOC, a spin polarization can be induced when the inversion symmetry is broken. Normally, sputtered HMs like Pt and Ta have a global inversion symmetry despite the fact that there is no microscopic symmetry due to the amorphous or polycrystalline nature of these materials. Therefore, they cannot allow for a net spin polarization in the bulk form. However, when an HM is interfacing to an FM like Co or CoFeB, the inversion symmetry is broken and at the interface, spin polarizations can be induced by applying an electric current in the interface plane. This effect can also be understood using a Rashba picture: at the interface, there is a vertical electric field \mathbf{E}_z along the out-of-film-plane direction; when an in-plane electric current is applied, there is an induced spin accumulation $\boldsymbol{\sigma} \propto \mathbf{j} \times \mathbf{E}_z$,³⁹ which is orthogonal to both

the out-of-plane direction and the current direction. While we here describe the effect of current-induced spin polarization using a Rashba picture, in reality, the effect can be due to spin Hall effect, Rashba effect, and Dresselhaus effect, where the latter two are also called inverse spin galvanic effect.⁵ Note that since there is a rotation symmetry in the film plane, the current-induced out-of-plane spin polarization is not allowed as we will describe below.

Crystal Symmetry and SOT

It is essential to determine the impact of crystal symmetry on the SOTs of 2D/FM materials for the SOT prediction. Since DL- and FL-SOTs ($\vec{\tau}_{\text{DL}}$ and $\vec{\tau}_{\text{FL}}$) are directly related to σ by following $\tau_{\text{DL}}\mathbf{m} \times (\mathbf{m} \times \sigma)$ and $\tau_{\text{FL}}\mathbf{m} \times \sigma$, respectively, we will determine the current-induced spin polarization using symmetry arguments. Conventional SOTs refer to SOTs resulting from the in-plane spin polarization, while the unconventional SOTs refer to SOTs resulting from the out-of-plane spin polarization. We adopt two methods, one is referred to as symmetry operation analysis which was used by MacNeil *et al.*¹⁰ and the other one is referred to as symmetry matrix analysis which was used by He and Law,⁴⁰ for determining the current-induced spin polarization using symmetry arguments.

Inversion Symmetry

We mentioned above that current-induced spin polarizations cannot exist when the inversion symmetry is preserved. This can be understood using the symmetry operation analysis: the spin polarization is a pseudovector that does not change sign and electric field (current) is a vector that changes sign under an inversion operation. In other words, the inversion symmetry leads to $\sigma \rightarrow \sigma$ and $\mathbf{j} \rightarrow -\mathbf{j}$, where \mathbf{j} is the applied electric current. Since the induced spin polarization is proportional to current to the first order ($\sigma \propto \mathbf{j}$), $\sigma \propto -\mathbf{j}$ under

Table 1: Magnetolectric pseudotensor χ in spin-orbit coupled material/globally high-symmetry FM thin film heterostructures with different group symmetries.⁴⁰ The principle axis is along z axis.

Point Group	χ	Point Group	χ
C_1	$\begin{pmatrix} \chi_{xx} & \chi_{xy} & \chi_{xz} \\ \chi_{yx} & \chi_{yy} & \chi_{yz} \\ \chi_{zx} & \chi_{zy} & \chi_{zz} \end{pmatrix}$	C_2	$\begin{pmatrix} \chi_{xx} & \chi_{xy} & 0 \\ \chi_{yx} & \chi_{yy} & 0 \\ 0 & 0 & \chi_{zz} \end{pmatrix}$
C_3	$\begin{pmatrix} \chi_{xx} & \chi_{xy} & 0 \\ \chi_{yx}[=-\chi_{xy}] & \chi_{yy}[=\chi_{xx}] & 0 \\ 0 & 0 & \chi_{zz} \end{pmatrix}$	C_4	$\begin{pmatrix} \chi_{xx} & \chi_{xy} & 0 \\ \chi_{yx}[=-\chi_{xy}] & \chi_{yy}[=\chi_{xx}] & 0 \\ 0 & 0 & \chi_{zz} \end{pmatrix}$
C_6	$\begin{pmatrix} \chi_{xx} & \chi_{xy} & 0 \\ \chi_{yx}[=-\chi_{xy}] & \chi_{yy}[=\chi_{xx}] & 0 \\ 0 & 0 & \chi_{zz} \end{pmatrix}$	C_S	$\begin{pmatrix} 0 & \chi_{xy} & 0 \\ \chi_{yx} & 0 & \chi_{yz} \\ 0 & \chi_{zy} & 0 \end{pmatrix}$
C_{2v}	$\begin{pmatrix} 0 & \chi_{xy} & 0 \\ \chi_{yx} & 0 & 0 \\ 0 & 0 & 0 \end{pmatrix}$	C_{3v}	$\begin{pmatrix} 0 & \chi_{xy} & 0 \\ \chi_{yx}[=-\chi_{xy}] & 0 & 0 \\ 0 & 0 & 0 \end{pmatrix}$
C_{4v}	$\begin{pmatrix} 0 & \chi_{xy} & 0 \\ \chi_{yx}[=-\chi_{xy}] & 0 & 0 \\ 0 & 0 & 0 \end{pmatrix}$	C_{6v}	$\begin{pmatrix} 0 & \chi_{xy} & 0 \\ \chi_{yx}[=-\chi_{xy}] & 0 & 0 \\ 0 & 0 & 0 \end{pmatrix}$
D_{2d}	$\begin{pmatrix} \chi_{xx} & 0 & 0 \\ 0 & \chi_{yy}[=-\chi_{xx}] & 0 \\ 0 & 0 & 0 \end{pmatrix}$	S_4	$\begin{pmatrix} \chi_{xx} & \chi_{xy} & 0 \\ \chi_{yx}[=\chi_{xy}] & \chi_{yy}[=-\chi_{xx}] & 0 \\ 0 & 0 & 0 \end{pmatrix}$
D_2	$\begin{pmatrix} \chi_{xx} & 0 & 0 \\ 0 & \chi_{yy} & 0 \\ 0 & 0 & \chi_{zz} \end{pmatrix}$	D_3	$\begin{pmatrix} \chi_{xx} & 0 & 0 \\ 0 & \chi_{yy}[=\chi_{xx}] & 0 \\ 0 & 0 & \chi_{zz} \end{pmatrix}$
D_4	$\begin{pmatrix} \chi_{xx} & 0 & 0 \\ 0 & \chi_{yy}[=\chi_{xx}] & 0 \\ 0 & 0 & \chi_{zz} \end{pmatrix}$	D_6	$\begin{pmatrix} \chi_{xx} & 0 & 0 \\ 0 & \chi_{yy}[=\chi_{xx}] & 0 \\ 0 & 0 & \chi_{zz} \end{pmatrix}$
T	$\begin{pmatrix} \chi_{xx} & 0 & 0 \\ 0 & \chi_{yy}[=\chi_{xx}] & 0 \\ 0 & 0 & \chi_{zz}[=\chi_{xx}] \end{pmatrix}$	O	$\begin{pmatrix} \chi_{xx} & 0 & 0 \\ 0 & \chi_{yy}[=\chi_{xx}] & 0 \\ 0 & 0 & \chi_{zz}[=\chi_{xx}] \end{pmatrix}$

inversion. Therefore, $\boldsymbol{\sigma}=0$ to the linear order. The second way to understand this is by using general symmetry analysis. The induced spin polarization vector ($\boldsymbol{\sigma}$) will be $\boldsymbol{\sigma} = \chi\mathbf{j}$, where χ is the 3D magnetoelectric pseudotensor. If a system has a set of symmetry operations $\{R\}$, then χ should respect

$$\chi = \det(R_i)R_i\chi R_i^T, R_i \in \{R\} \quad (3)$$

where R_i is the arbitrary symmetry operation in the set, $\det(R_i)$ is its determinant, and R_i^T is its transpose ($R_i R_i^T=1$). For readers who are not familiar with symmetry groups, illustrations of symmetry groups can be found on reference⁴¹ and all symmetry operations of a point group can be easily found on reference.⁴² To calculate the most general form of χ , we first assume that

$$\chi = \begin{pmatrix} \chi_{xx} & \chi_{xy} & \chi_{xz} \\ \chi_{yx} & \chi_{yy} & \chi_{yz} \\ \chi_{zx} & \chi_{zy} & \chi_{zz} \end{pmatrix} \quad (4)$$

where 9 elements in the tensor can be all arbitrary. We then calculate χ by substituting Eq. 4 and R_i into Eq. 3. To validate the equation, some elements of χ will have to be zero and thus are not allowed by the symmetry operation R_i . As shown by He and Law,⁴⁰ only 18 point groups allow for a non-zero spin accumulation in the presence of a charge current (see Table 1). These 18 point groups are non-centrosymmetric since a net spin accumulation is not allowed in a system with inversion symmetry. Since the inversion symmetry operation matrix is given by

$$i = \begin{pmatrix} -1 & 0 & 0 \\ 0 & -1 & 0 \\ 0 & 0 & -1 \end{pmatrix}$$

Eq. 4 under the inversion symmetry becomes:

$$\begin{pmatrix} \chi_{xx} & \chi_{xy} & \chi_{xz} \\ \chi_{yx} & \chi_{yy} & \chi_{yz} \\ \chi_{zx} & \chi_{zy} & \chi_{zz} \end{pmatrix} = \det(i)\chi i^T = - \begin{pmatrix} \chi_{xx} & \chi_{xy} & \chi_{xz} \\ \chi_{yx} & \chi_{yy} & \chi_{yz} \\ \chi_{zx} & \chi_{zy} & \chi_{zz} \end{pmatrix} \implies \begin{pmatrix} \chi_{xx} & \chi_{xy} & \chi_{xz} \\ \chi_{yx} & \chi_{yy} & \chi_{yz} \\ \chi_{zx} & \chi_{zy} & \chi_{zz} \end{pmatrix} = 0 \quad (5)$$

Therefore, we see that the magnetoelectric tensor χ is zero for inversion symmetric systems. Note that for inversion symmetric systems, non-zero spin accumulations at the top and bottom surfaces with opposite signs can be induced in the presence of charge current. However, the net spin accumulation is zero as constrained by the inversion symmetry. In general, a spin Hall conductivity associated with the spin Hall effect is usually described by a rank-3 tensor^{43,44} and we need to reduce it to a rank-2 tensor by fixing the spin current direction to be out-of-plane direction if we want to continue the discussion as we do here. In the following, the impact of rotation, mirror, screw, and glide symmetries on SOTs will be discussed.

Mirror Symmetry

The mirror plane perpendicular to the z axis is broken in thin-film heterostructures. Thus, we only consider the cases where there are mirror planes parallel to the z axis of the heterostructure. When sending an in-plane current to the heterostructures, the simplified form of the torque can be expressed as:

$$\begin{aligned} \vec{\tau}_{\perp}(\mathbf{m}, E) &= \tau_{\perp}(\varphi, E)\mathbf{z} \\ \vec{\tau}_{\parallel}(\mathbf{m}, E) &= \tau_{\parallel}(\varphi, E)\mathbf{m} \times \mathbf{z}, \end{aligned} \quad (6)$$

where $\vec{\tau}_{\perp}(\mathbf{m}, E)$ and $\vec{\tau}_{\parallel}(\mathbf{m}, E)$ are the out-of-plane and in-plane torque vectors, E is the applied electric field, and φ is the azimuth angle between the magnetization vector \mathbf{m} and the x axis as shown in Fig. 2. Here, we assume that the magnetization is in the film plane.

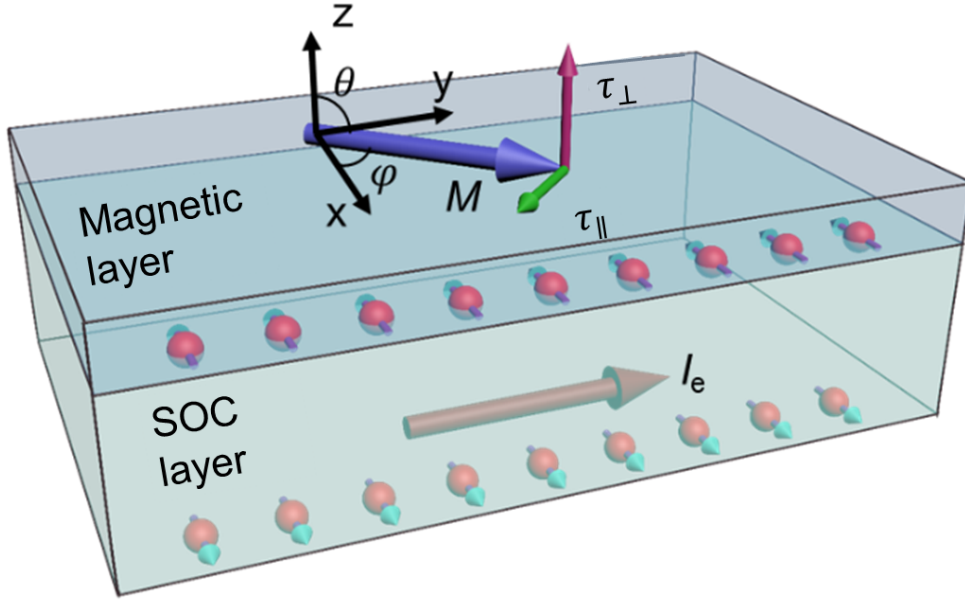


Figure 2: Schematic of a nonmagnetic spin-orbit coupled (SOC) layer/magnetic layer heterostructures for symmetry analysis of current-induced SOTs. Assuming that the current is flowing along the y direction, the angle between magnetization and x direction is azimuthal angle φ and the angle between magnetization and z direction is polar angle θ . The red balls represent the electrons and the arrows represent the spin direction. Here, only conventional in-plane spin polarization and corresponding in-plane DL-SOT (τ_{\parallel}) and out-of-plane FL-SOT (τ_{\perp}) are illustrated.

For cases where magnetization is out-of-plane, the symmetry operation analysis is similar except that the out-of-plane and in-plane torques are replaced by two orthogonal in-plane torques. The scalar-prefactor $\tau_{\perp}(\varphi, E)$ and $\tau_{\parallel}(\varphi, E)$ can be Fourier expanded as¹⁰:

$$\begin{aligned}\tau_{\perp}(\varphi, E) &= E(A_0 + A_1\sin\varphi + A_2\cos\varphi + A_3\sin 2\varphi + A_4\cos 2\varphi + \dots) \\ \tau_{\parallel}(\varphi, E) &= E(S_0 + S_1\sin\varphi + S_2\cos\varphi + S_3\sin 2\varphi + S_4\cos 2\varphi + \dots),\end{aligned}\tag{7}$$

where A_1 and S_1 represent the linear-order conventional FL- and DL-SOTs, respectively, due to the in-plane spin polarization and A_0 and S_0 represent the unconventional DL- and FL-SOTs, respectively, due to the out-of-plane spin polarization. One can re-write Eq. 6 to obtain the symmetry transformation:

$$\begin{aligned}\tau_{\perp}(\varphi, E) &= \vec{\tau}_{\perp} \cdot \mathbf{z} \\ \tau_{\parallel}(\varphi, E) &= \vec{\tau}_{\parallel} \cdot (\mathbf{m} \times \mathbf{z}).\end{aligned}\tag{8}$$

For a lattice that preserves a mirror plane M_{xz} perpendicular to the y axis, the mirror symmetry operation reverses the x component of magnetization leading to $\varphi \rightarrow \pi - \varphi$ as shown in Fig. 2. When sending an in-plane current along the y direction, the electric field flips sign denoting as $E \rightarrow -E$. Since the dot and cross products of a pseudovector and a vector are pseudovector and vector, respectively, $\vec{\tau}_{\perp} \cdot \mathbf{z}$ transforms to $-\vec{\tau}_{\perp} \cdot \mathbf{z}$ and $\vec{\tau}_{\parallel} \cdot (\mathbf{m} \times \mathbf{z})$ transforms to $-\vec{\tau}_{\parallel} \cdot (\mathbf{m} \times \mathbf{z})$ under the mirror symmetry. Therefore, the mirror symmetry requires:

$$\begin{aligned}\tau_{\perp}(\pi - \varphi, -E) &= -\tau_{\perp}(\varphi, E) \\ \tau_{\parallel}(\pi - \varphi, -E) &= -\tau_{\parallel}(\varphi, E)\end{aligned}\tag{9}$$

To fulfill the requirements of Eq. 9, Eq. 6 is reduced to:

$$\begin{aligned}\tau_{\perp} &= E(A_0 + A_1\sin\varphi + A_3\sin 2\varphi + \dots), \\ \tau_{\parallel} &= E(S_0 + S_1\sin\varphi + S_3\sin 2\varphi + \dots).\end{aligned}\tag{10}$$

A_0, A_1, S_0 and S_1 are not reduced in the above equation which suggests that both conventional and unconventional torques are allowed if only M_{xz} exists and the current is along the y direction.

Now, if the lattice also preserves a mirror plane M_{yz} perpendicular to the x axis, the symmetry transformation rules are: (1) $\varphi \rightarrow -\varphi$; (2) $E \rightarrow E$ and (3) $\vec{\tau}_{\perp} \cdot \mathbf{z} \rightarrow -\vec{\tau}_{\perp} \cdot \mathbf{z}$ and $\vec{\tau}_{\parallel} \cdot (\mathbf{m} \times \mathbf{z}) \rightarrow -\vec{\tau}_{\parallel} \cdot (\mathbf{m} \times \mathbf{z})$. The additional symmetry constraints caused by M_{yz} are

$$\begin{aligned}\tau_{\perp}(\varphi, E) &= -\tau_{\perp}(-\varphi, E) \\ \tau_{\parallel}(\varphi, E) &= -\tau_{\parallel}(-\varphi, E).\end{aligned}\tag{11}$$

Applying Eq. 9 and 11 to Eq. 6, one obtains

$$\begin{aligned}\tau_{\perp} &= E(A_1\sin\varphi + A_3\sin 2\varphi + \dots) \\ \tau_{\parallel} &= E(S_1\sin\varphi + S_3\sin 2\varphi + \dots)\end{aligned}\tag{12}$$

As can be seen, A_0 and S_0 no longer exist. This result suggests that the unconventional torques would not exist in a crystal lattice having mirror planes perpendicular to both x and y axis. Here we only derive the case for the angle between the mirror planes are 90 degrees. To generate the unconventional SOTs, the applied in-plane current direction also matters. Eq. 10 describes the case that only one mirror plane (M_{xz}) exists and the applied current is perpendicular to M_{xz} plane, where unconventional SOTs are allowed. Now, let's consider the case when the lattice still only preserves the mirror plane M_{xz} and the current is applied parallel to M_{xz} (along the x axis). The current does not change sign under reflection. Eq. 7

will reduce to

$$\begin{aligned}\tau_{\perp} &= E(A_2\cos\varphi + A_4\cos2\varphi + \dots) \\ \tau_{\parallel} &= E(S_2\cos\varphi + S_4\cos2\varphi + \dots)\end{aligned}\tag{13}$$

if the symmetry transformations are applied. Unconventional SOTs disappear in this case. Hence, when there is only one mirror plane perpendicular to the xy plane, the applied in-plane current should be perpendicular to the mirror plane for generating unconventional SOTs.

One can also understand the impact of mirror symmetry on the SOT from the spin accumulation matrix under mirror operations. The mirror symmetry operation matrix with respect to the xz plane is given by

$$M_{xz} = \begin{pmatrix} 1 & 0 & 0 \\ 0 & -1 & 0 \\ 0 & 0 & 1 \end{pmatrix}$$

According to Eq. 3 and 4, χ respects:

$$\begin{aligned}\begin{pmatrix} \chi_{xx} & \chi_{xy} & \chi_{xz} \\ \chi_{yx} & \chi_{yy} & \chi_{yz} \\ \chi_{zx} & \chi_{zy} & \chi_{zz} \end{pmatrix} &= \det(M_{xz})M_{xz}\chi M_{xz}^T = \begin{pmatrix} -\chi_{xx} & \chi_{xy} & -\chi_{xz} \\ \chi_{yx} & -\chi_{yy} & \chi_{yz} \\ -\chi_{zx} & \chi_{zy} & -\chi_{zz} \end{pmatrix} \\ &\implies \chi = \begin{pmatrix} 0 & \chi_{xy} & 0 \\ \chi_{yx} & 0 & \chi_{yz} \\ 0 & \chi_{zy} & 0 \end{pmatrix}\end{aligned}\tag{14}$$

Therefore, the electric field along x direction can't induce spin polarization along z direction when a mirror plane with respect to the xz plane presents. In contrast, the electric field along y direction can induce spin polarization along z direction. These conclusions drawn by using symmetry matrix analysis are consistent with ones drawn by using symmetry operation analysis. Here we only derive the case for the angle between the mirror

planes are 90 degrees. Actually, no matter what the angle between these mirror planes, the unconventional SOTs would not exist if two intersecting mirror planes perpendicular to the xy plane is found. Because there must be a rotation axis about the intersection line of these mirror planes. As it will be shown later that if there is a rotation axis about the z axis in the lattice, the unconventional SOTs would not exist.

Rotation Symmetry

The rotation symmetries about the x and y axis are broken in 2D/FM heterostructures, but rotation symmetry about z axis may still exist. We use the same method to analyze the impact of rotation symmetries about z axis. In a lattice preserving a 2-fold rotation symmetry about the z axis, the symmetry transformation leads to: (1) $\varphi \rightarrow \pi + \varphi$; (2) $E \rightarrow -E$ and (3) $\vec{\tau}_\perp \cdot \mathbf{z} \rightarrow \vec{\tau}_\perp \cdot \mathbf{z}$ and $\vec{\tau}_\parallel \cdot (\mathbf{m} \times \mathbf{z}) \rightarrow \vec{\tau}_\parallel \cdot (\mathbf{m} \times \mathbf{z})$. Applying these symmetry transformations to Eq. 7, one obtains,

$$\begin{aligned}\tau_\perp &= E(A_1 \sin\varphi + A_2 \cos\varphi + \dots) \\ \tau_\parallel &= E(A_1 \sin\varphi + A_2 \cos\varphi + \dots)\end{aligned}\tag{15}$$

Similar results apply to all n -fold ($n > 2$) rotation symmetries. Hence, the rotation symmetry about the z axis will eliminate the unconventional torque.

Alternatively, we can use

$$\chi_{\{R\}} = \chi + \sum_{(R_i \in \{R\})} \det(R_i) R_i \chi R_i^T\tag{16}$$

to directly find the χ that satisfies $\{R\}$. Besides the fact that some elements are not allowed by symmetry operations, some elements of χ are required to be same or opposite. For

example, for a C_3 point group,

$$\begin{aligned} \chi_{C_3} &= \chi + \det(C_3)C_3\chi C_3^T + \det[(C_3)^2][(C_3)^2]\chi[(C_3)^2]^T \\ &= \begin{pmatrix} \frac{3}{2}(\chi_{xx} + \chi_{yy}) & \frac{3}{2}(\chi_{xy} - \chi_{yx}) & 0 \\ -\frac{3}{2}(\chi_{xy} - \chi_{yx}) & \frac{3}{2}(\chi_{xx} + \chi_{yy}) & 0 \\ 0 & 0 & 3\chi_{zz} \end{pmatrix} \implies \chi = \begin{pmatrix} \chi_{xx} & \chi_{xy} & 0 \\ \chi_{yx}[-\chi_{xy}] & \chi_{yy}[=\chi_{xx}] & 0 \\ 0 & 0 & \chi_{zz} \end{pmatrix}, \end{aligned} \quad (17)$$

where C_3 is the matrix for 120-degree rotation along the z axis and $(C_3)^2$ is for 240-degree rotation. From this example, we see that we can get relations between different elements; some must be the same and some must be the opposite according to the symmetry operations.

We can derive χ of a specific point group by applying all symmetry operations in the set of the point group symmetry operations. In Table 1, the definition of point group follows Schoenflies notation and we can obtain the current-induced spin polarization for materials with any arbitrary symmetry point group. Amorphous or polycrystalline HM/FM heterostructures can be effectively treated as $C_{\infty v}$, which is not a legitimate point group for crystalline materials according to a crystallographic restriction theorem. $C_{\infty v}$ shares the same χ with C_{nv} ($n > 2$) and only allows two elements: χ_{xy} and $\chi_{yx}(=-\chi_{xy})$. Therefore, the current-induced spin polarization can only lie in the film plane for HM/FM heterostructures.

Screw and Glide Symmetry

An n -fold screw rotation can be decomposed of an n -fold rotation and a translation about the rotation axis as shown in Fig. 3 (a). As a result, the screw symmetry about the z axis in a 2D material eliminates the unconventional SOT. Fortunately, all kinds of screw symmetries are broken after interfacing to an FM, since rotation symmetries about the x

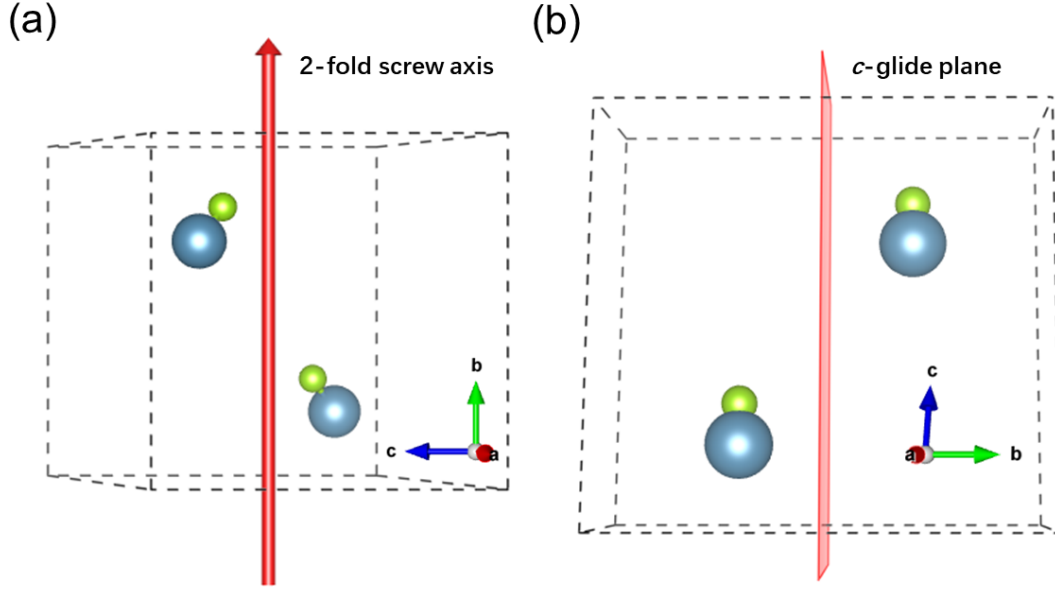


Figure 3: Schematics of screw and glide symmetry. (a) Unit cell of a lattice that preserves the 2-fold screw rotation. (b) Unit cell of a lattice that preserves the c -glide symmetry.

and y axis and the translation symmetry about the z axis are broken after interfacing to an FM. It is worth noting that the screw symmetry may help understand the layer dependence of current induced spin polarization^{10,45} which will be introduced later.

A glide plane can be decomposed of a mirror and a translation as shown in Fig. 3 (b). There are a -, b -, c -, n - and d - glide planes where the Latin letter represents the translation direction. Note that we first identify glide symmetries that could exist in the 2D/FM heterostructures. Whether the glide symmetry is broken or not after the 2D material interfacing to an FM can be determined by two conditions: (i) the glide plane is parallel to the 2D/FM interface; and (ii) the glide operation involves a translation along the z axis. If either of the conditions is fulfilled, the glide plane symmetry is considered broken after the 2D material interfacing to an FM. Now we check every glide symmetry with these conditions.

Assuming the $c(a, b)$ axis of the lattice is along the $z(x, y)$ direction. Since the mirror plane perpendicular to the z axis is broken after interfacing to an FM, glide planes perpendicular to z axis are also broken in 2D/FM. Hence, only glide planes perpendicular to the x or y

axis need to be considered. c -, n - and d - glide planes perpendicular to the x or y axis involve translations along the z direction, hence these glide planes are also broken after interfacing to an FM. The mirror plane that is perpendicular to x or y axis can still be preserved after interfacing to an FM, so a - (b -) glide plane perpendicular to y (x) axis doesn't fulfill the condition (i). Meanwhile, these glides planes don't involve translations along the z axis, so the condition (ii) is also not satisfied. Therefore, a - (b -) glide plane perpendicular to y (x) axis can be preserved after interfacing to an FM. And it can be treated as the mirror plane perpendicular to the x or y axis.

Unconventional SOT Prediction

2D materials provide an opportunity to generate a desirable spin polarization thanks to their diverse symmetry properties and strong SOC. Using the above methods, we can predict if unconventional SOTs are allowed or not in 2D/FM heterostructures. To allow unconventional SOTs the crystal lattice of 2D materials should satisfy the following conditions: (i) no n -fold rotation ($n > 1$) axis about the surface normal direction (z axis) exists; (ii) the lattice preserves at most one mirror plane or glide plane (a - or b -glide) perpendicular to an in-plane axis. Fortunately, the needed symmetry information is already contained in the space group notation of the material. One can conveniently grab the symmetry elements about the characteristic direction of the lattice from the material's Hermann–Mauguin notation. Table 2 lists space groups for common 2D materials. The crystal structure, characteristic axis and the symmetry elements for various 2D materials are shown in Fig. 4. In the following, we use two examples to illustrate how to determine if the unconventional SOTs are allowed.

First, we take 1T MoSe₂ with a space group of R3m and SnS with a space group of Pnma as examples. The crystal structures of SnS and MoSe₂ are shown in Fig. 4(c) and (f). The full space group notation of MoSe₂ is R3m which has a trigonal lattice structure. As shown in Fig. 4(c), the characteristic crystal axis c is along the z direction and perpendicular to the a

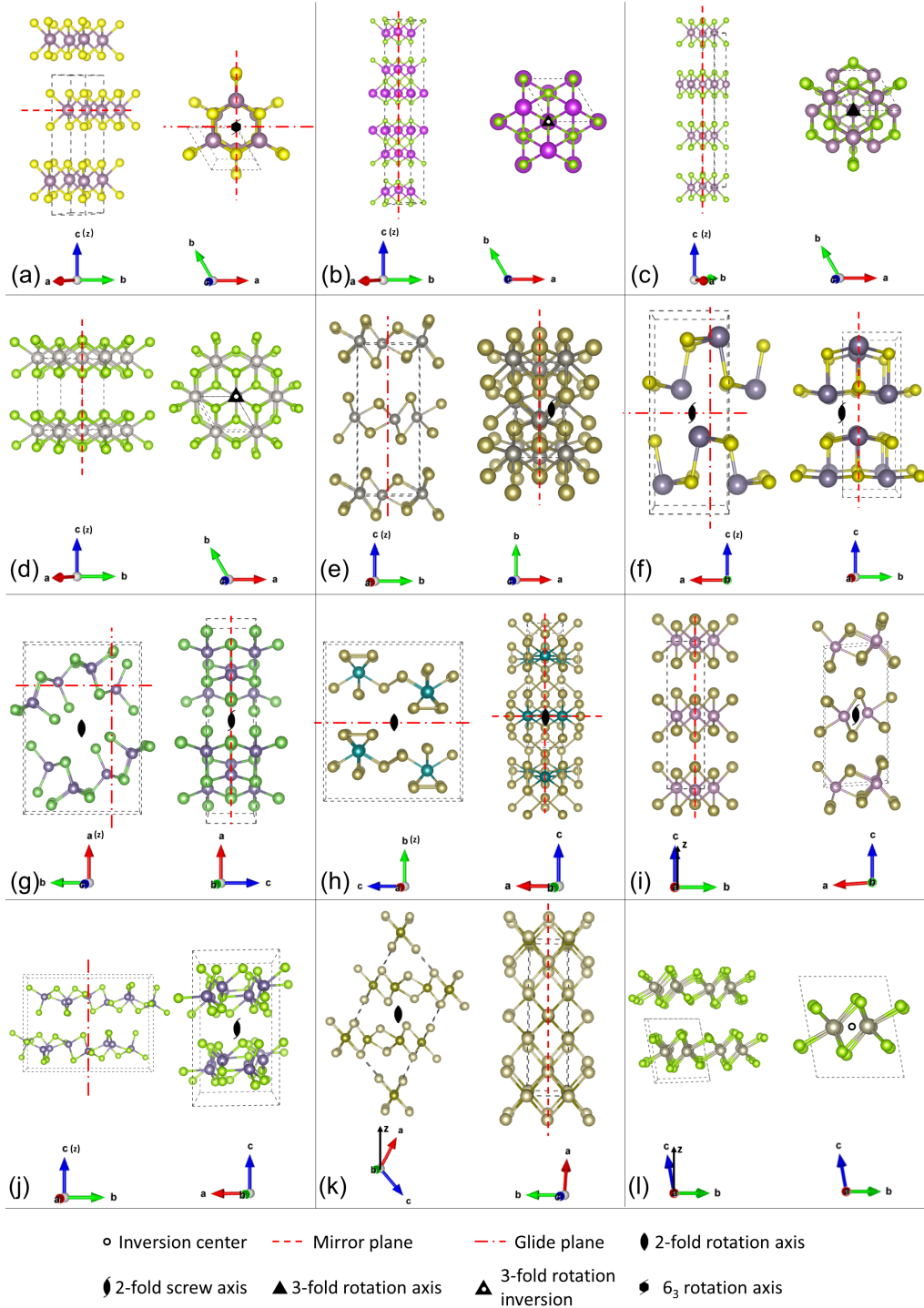


Figure 4: The crystal structure, characteristic axis and the symmetry elements lying with the characterization axis of various 2D materials. (a)MoS₂ (P6₃/mmc), (b)Bi₂Se₃ (R $\bar{3}$ m), (c)MoSe₂ (R3m), (d)PtSe₂ (P $\bar{3}$ m1), (e)WTe₂ (Pmn2₁), (f)SnS (Pnma), (g)GeAs₂ (Pbam), (h)HfTe₅ (Cmcm), (i)MoTe₂ (P2₁/m), (j) β GeSe₂ (P2₁/c), (k)TaTe₂ (C2/m), (l)ReSe₂ (P $\bar{1}$). a , b and c arrows represent the characteristic axis directions of the lattice, z axis represents the surface normal direction.

and b axis. The angle between a and b axis is 120 degrees and they have the same symmetry operations. The space group notation shows there is a 3-fold rotation axis about the c axis so that condition (i) is not satisfied. Besides, there are two mirror planes perpendicular to a and b axis, respectively. Therefore, condition (ii) is not satisfied either. For its a and b axis, there is a mirror plane perpendicular to them, respectively. Hence, unconventional SOTs are not allowed in 1T MoSe₂ with a space group of R3m.

The full space group notation of SnS is P2₁/n2₁/m2₁/a, the space group notation implies

Table 2: The full space group notation of various 2D materials, the point group for the 2D material (2D/FM) and unconventional SOT predictions.

2D materials	Space group of 2D	2D/FM	Unconventional τ_{DL}
Black Phosphorous	C2/m 2/c 2 ₁ /a ⁴⁶	C _{2v}	N
SnS, SnSe, GeS, GeSe	P2 ₁ /n 2 ₁ /m 2 ₁ /a ^{46,47}	C _{1v}	Y
GeAs ₂	P2 ₁ /b 2 ₁ /a 2/m ⁴⁶	C _{1v}	Y
SiP	C2/m 2/c 2 ₁ ⁴⁷	C _{1v}	Y
GaP, GeAs, GeTe	C1 2/m 1 ^{46,47}	C _{1v}	Y
GeS ₂ , β -GeSe ₂ , MoO ₂	P1 2 ₁ /c 1 ⁴⁶	C ₁	Y
TiS ₃ , TiSe ₃ , ZrS ₃ , ZrSe ₃ , HfS ₃ , HfSe ₃	P1 2 ₁ /m 1 ^{46,47}	C ₁	Y
2H-NbSe ₂ , MoS ₂ , MoSe ₂ , WS ₂ , WSe ₂ , MoTe ₂ , SnSe ₂	P6 ₃ /m 2/m 2/c ⁴⁸	C _{3v}	N
1T-MoS ₂ , MoSe ₂ , WS ₂ , WSe ₂ , MoTe ₂ , SnSe ₂	P $\bar{3}$ 2/m 1 ⁴⁸	C _{3v}	N
1T'-MoS ₂ , MoSe ₂ , WS ₂ , WSe ₂ , MoTe ₂ , SnSe ₂	P1 2 ₁ /m 1 ⁴⁸	C _{1v}	Y
3R-MoS ₂ , MoSe ₂ , WS ₂ , WSe ₂ , MoTe ₂ , SnSe ₂	R3m ⁴⁸	C _{3v}	N
1T'-ReSe ₂ , ReS ₂	P $\bar{1}$ ⁴⁸	C ₁	Y
T _d -MoS ₂ , T _d -MoTe ₂ , T _d -WTe ₂ , TaIrTe ₄	Pmn2 ₁ ^{10,47}	C _{1v}	Y
Bi ₂ Se ₃ , Bi ₂ Te ₃ , Sb ₂ Te ₃ , Sb ₂ Se ₃	R $\bar{3}$ 2/m ⁴⁹	C _{3v}	N
1T'-TaTe ₂ , NbTe ₂	C1 2/m 1 ^{25,50}	C _{1v}	Y
PtSe ₂ , PtTe ₂ , PdTe ₂ , PtBi ₂	P $\bar{3}$ 2/m 1 ⁵¹	C _{3v}	N
ZrTe ₅ , HfTe ₅ , Ta ₂ NiS ₅	C2/m 2/c 2 ₁ /m ⁵²	C _{2v}	N
TlSe	I4/m 2/c 2/m ⁴⁷	C _{2v}	N

that the crystal has an orthorhombic lattice structure. The characteristic crystal directions a , b and c are perpendicular to each other as shown in Fig. 4(f). About the c axis (z axis), $2_1/a$ suggests that there are a 2-fold screw axis and an a -glide plane perpendicular to it. About the a axis (x axis), $2_1/n$ suggests that there are a 2-fold screw axis and an n -glide plane perpendicular to it. About the b axis (y axis), $2_1/m$ suggests that there are a 2-fold screw axis and a mirror plane perpendicular to it. We need to check conditions (i) and (ii) to determine if unconventional SOTs are allowed. For SnS, the crystal c axis is along z axis and there is no rotation axis along c axis as indicated by the space group notation. Condition (i) is satisfied. In SnS, only one mirror plane perpendicular to the b axis as indicated by the space group notation. Condition (ii) is satisfied. Hence, unconventional SOTs are allowed in SnS by symmetry.

The symmetry matrix analysis is very useful for theoretical calculations. To predict unconventional SOTs with the symmetry matrix, the point group of the 2D/FM heterostructure needs to be determined since the integration could break some symmetry operations of the 2D materials. We then obtain the corresponding magnetoelectric pseudovector using Table 1 according to the point group. Table 2 summarizes the point groups for various 2D/FM bilayers and our predictions about the existence of unconventional SOTs.

Review of the Experimental Progress

Since the inversion symmetry in 2D/FM heterostructures is broken, we expect an in-plane spin accumulation, an FL-SOT in the form of $\boldsymbol{\tau}_{\text{FL}} \propto \mathbf{m} \times (\mathbf{z} \times \mathbf{j})$ and a DL-SOT in the form of $\boldsymbol{\tau}_{\text{DL}} \propto \mathbf{m} \times [\mathbf{m} \times (\mathbf{z} \times \mathbf{j})]$. As argued above, an out-of-plane spin polarization can be expected in heterostructures with lateral symmetry breaking. As a result, unconventional DL- and FL-SOTs could be found. To compare experiment results from the literature, we use SOT efficiency (ξ) and spin conductivity (σ), which are defined by SOT efficiency

$\xi = (2e/\hbar)J_S/J_C$ (J_S : spin current density, J_C : charge current density) and spin conductivity $\sigma = J_S/E$ (E : electric field), respectively. These two values differ by a factor of the electrical conductivity (σ_C) of the SOC material: $\xi = (2e/\hbar)\sigma/\sigma_C$. SOT efficiencies of conventional FL-SOT (τ_A), DL-SOT (τ_S), unconventional FL-SOT (τ_T), and DL-SOT (τ_B) are expressed as ξ_A , ξ_S , ξ_T , and ξ_B , respectively. Their spin conductivities are expressed as σ_A , σ_S , σ_T , and σ_B , respectively.

Topological Insulators

In search of materials to provide efficient SOTs, TIs such as the Bi_2Se_3 family are among the most promising candidates owing to its helical spin structure (spin-momentum locking) of the topological surface states (TSSs). Earlier reviews that mention or focus on spintronics based on TIs include refs..^{5,53–55} Here, we summarize recent experimental progress of TI-based SOT devices that are highly tunable or compatible with CMOS technology. It is worth mentioning that the discussion in this section is limited to conventional SOTs. Because unconventional SOTs in these materials are not allowed by symmetry according to the previous symmetry analysis as shown in Table 2. Note that this review focuses on TIs that are 2D materials.

Tuning SOTs from TIs. Carrier density of TSSs plays a crucial role in determining the SOT efficiency in a TI-based heterostructure. Experimentally, Fan *et al.*¹¹ have shown that the SOT strength can be tuned by a factor of four in a Cr-doped TI device with a top gate voltage. The TI device shows the largest SOT efficiency when the carrier density of the top surface is close to the minimum and the overall surface state carrier density reaches the maximum as shown in Fig. 5 (a). Tuning carrier density of TSSs by varying the Bi:Sb ratio in $(\text{Bi}_{1-x}\text{Sb}_x)_2\text{Te}_3$ has been shown by Wu *et al.*⁵⁶ As shown in Fig. 5 (b), the maximum SOT effective field is also found when the Fermi level is close to the Dirac point and the transport signatures are dominated by the TSSs. Note that Kondou *et al.*⁵⁹ showed that the

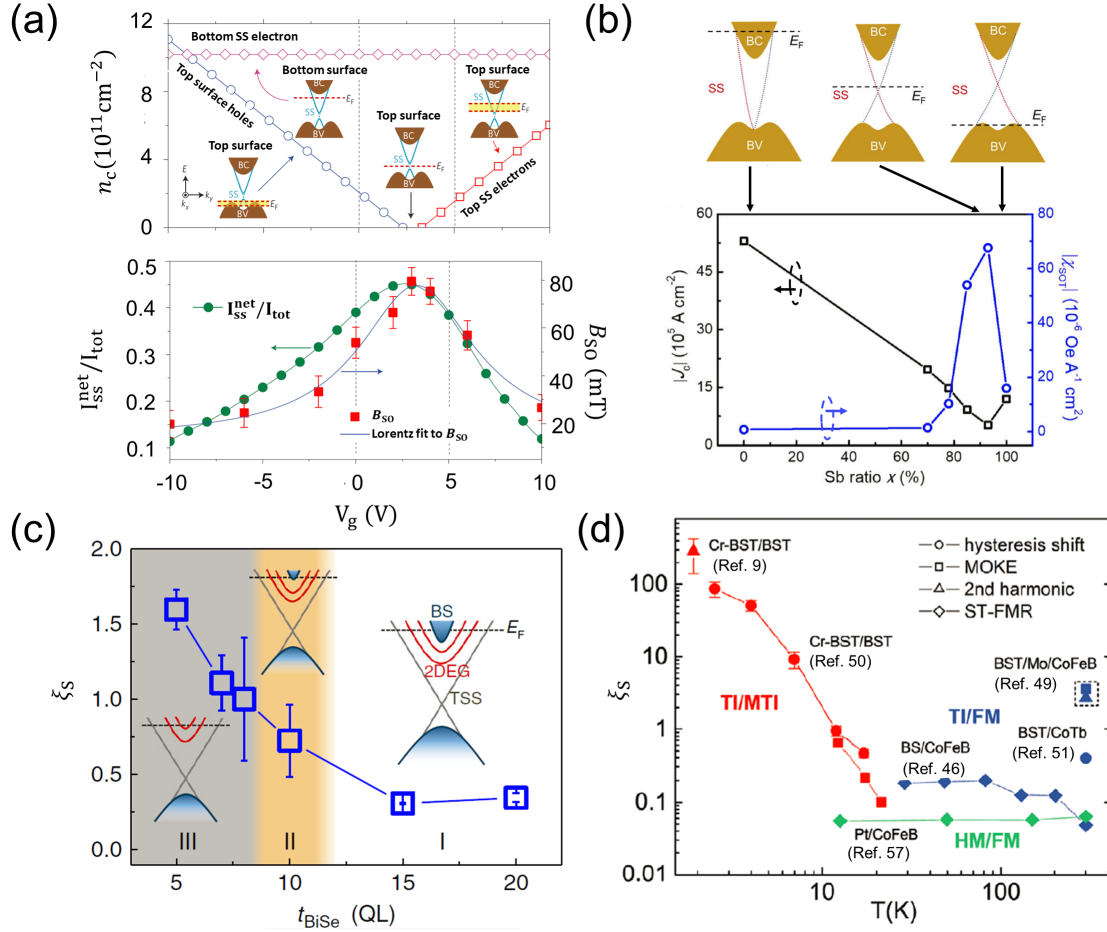


Figure 5: Tuning SOTs from TIs through electric field, composition, thickness, and temperature. (a) Control the Fermi level and the carrier density n_C by electric fields. The upper panel shows the top and bottom surface carrier densities as functions of gate voltage V_g . The lower panel shows the ratio between the net spin-polarized surface current over total current and the effective spin orbit field B_{SO} as functions of V_g . (b) The SOT effective field χ_{SOT} and switching current density as a function of Sb content. The Fermi level is indicated by the upper panel insets. (c) The SOT efficiency (ξ_S) as a function of Bi_2Se_3 thickness at room temperature. The inset shows the schematic of the band structure. (d) The ξ_S as a function of temperature for various devices. The figures are reproduced from Fan *et al.*,¹¹ Wu *et al.*,⁵⁶ Wang *et al.*⁵⁷ and Che *et al.*⁵⁸

SOT efficiency reaches the minimum when the Fermi level is close to the Dirac point, which was attributed to possible inhomogeneity of Dirac electron momentum and/or instability of the helical spin structure.

SOTs from TIs depend on the layer thickness. Wang *et al.*⁵⁷ have studied the SOT efficiency as a function of the TI thickness in a Bi₂Se₃/Py heterostructure as shown in Fig. 5 (c). The SOT efficiency increases with the decrease of TI thickness, resulting from decreasing bulk states and 2DEG states and increasing TSSs.

The SOT efficiency of TI based device is sensitive to the temperature. Che *et al.*⁵⁸ studied the temperature dependence of SOT of a TI/MTI device using the hysteresis shift and MOKE methods. The TI shows a much larger SOT efficiency when the temperature is below 12 K which is attributed to a higher spin polarization ratio of the TSS at low temperatures. The temperature dependence of spin Hall angle for various TI based devices is shown in Fig. 5 (d). It can be seen that the SOT efficiency of HM/FM device has a weak dependence on the temperature,⁶⁰ whereas the SOT efficiency of TI/MTI and TI/FM devices shows much higher values at low temperatures.

Room temperature perpendicular magnetization switching using TIs. A major challenge is to integrate a ferromagnetic layer with PMA on TI. Han *et al.*⁶¹ have shown SOT switching of perpendicular magnetized materials in Bi₂Se₃/ and (BiSb)₂Te₃/CoTb utilizing the strong bulk PMA of CoTb at room temperature as shown in Fig. 6 (a).

The PMA can also be achieved by inserting a metal layer between TI and a ferromagnetic layer. It is known that the Ta seed layer can promote PMA in CoFeB thin films since it absorbs boron increasing the crystallization of CoFeB. Mahendra *et al.*⁶² have obtained PMA in TI based heterostructures by inserting a thin Ta layer between Bi_xSe_{1-x} and CoFeB stack as shown in Fig. 6 (b). The required current density to switch the magnetization is only around $4.3 \times 10^5 \text{ Acm}^{-2}$. However, the drawback of inserting a heavy metal layer between TI and an FM layer is that the insertion layer hinders the spin current diffusion to the FM layer. To maintain a high SOT efficiency, inserting a light metal with a weak SOC strength

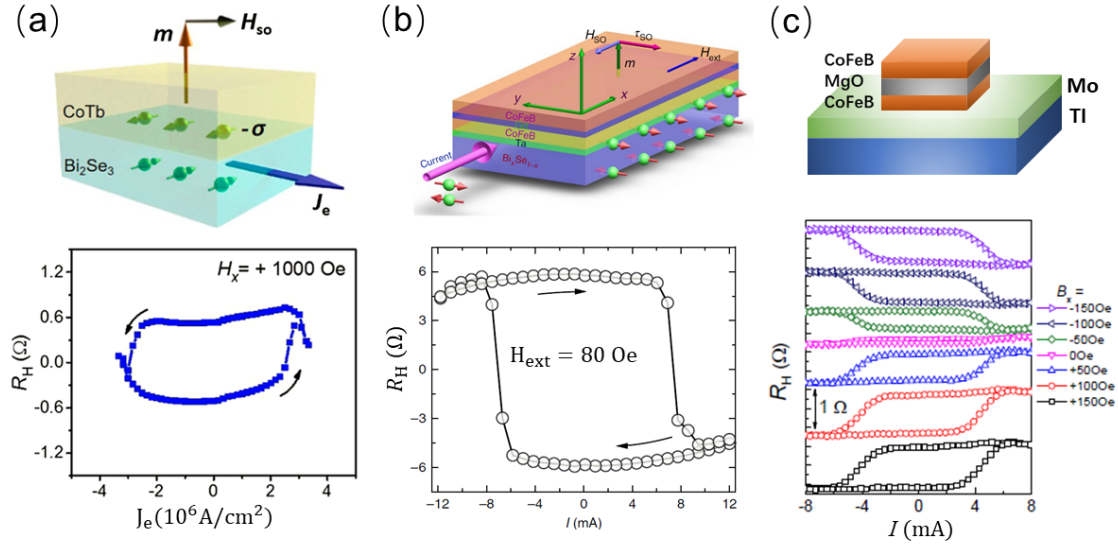


Figure 6: Current induced magnetization switching in TI/FM stacks with PMA: (a) $\text{Bi}_2\text{Se}_3/\text{CoTb}$, (b) $\text{Bi}_x\text{Se}_{1-x}/\text{Ta}(0.5\text{nm})/\text{CoFeB}/\text{Gd}/\text{CoFeB}$, and (c) $(\text{BiSb})_2\text{Te}_3/\text{Mo}(2\text{nm})/\text{CoFeB}$ stacks. The figures are reproduced from Han *et al.*⁶¹, Mahendra *et al.*⁶² and Shao *et al.*⁶³

could be a better option. Shao *et al.*⁶³ have shown current induced magnetization switching in $\text{Bi}_2\text{Se}_3/$, $\text{Bi}_2\text{Te}_3/$ and $(\text{BiSb})_2\text{Te}_3/\text{Mo}/\text{CoFeB}$ structures with PMA. The switching current for the $(\text{BiSb})_2\text{Te}_3/\text{Mo}/\text{CoFeB}$ device is as low as $3 \times 10^5 \text{ Acm}^{-2}$ and a large SOT efficiency of about 2.66 is obtained. The advantages of inserting a Mo layer are threefold: first, Mo has a weak SOC and does not significantly reduce the SOT efficiency; second, $\text{Mo}/\text{CoFeB}/\text{MgO}$ has a strong PMA at room temperature; third, Mo has a high thermal stability compared with Ta and thus is more compatible with modern CMOS technologies that require annealing temperature as high as 400°C .

To utilize TIs for future SOT-based devices, two important directions need to be pursued. First, since unconventional SOTs are not allowed in TI/FM heterostructures, methods to achieve reliable field-free switching for TI-based devices need to be investigated. Potential methods include a lateral structure asymmetry,⁸ tilted anisotropy,⁶⁴ and exchange bias.^{65,66} Second, since the high resistance of TIs could compensate for the advantage of TIs' high

SOT efficiency,⁶⁷ conductive TIs with giant SOTs are highly desirable. Promising results have been shown recently that a conductive TI Bi_{0.9}Sb_{0.1} was reported to host a very large SOT efficiency with a very low resistivity.⁶⁸

Table 3: The SOT efficiencies and spin conductivities of TI/FM heterostructures.

Authors	Materials	Characterization technique	ξ	$(\times 10^3 \frac{\sigma}{(\hbar/2e)(\Omega m)^{-1}})$	Note
Fan <i>et al.</i> ⁹	(BiSb) ₂ Te ₃ /Cr-(BiSb) ₂ Te ₃	SHH	$\xi_S=140-425$ $\xi_A=26$	$\sigma_S=1540-4675$ $\sigma_A=286$	measured at 1.9 K and magnetization angle dependent
Che <i>et al.</i> ⁵⁸	(BiSb) ₂ Te ₃ /Cr-(BiSb) ₂ Te ₃	Hysteresis shift MOKE	$\xi_S=0.1-100$		temperature dependent
Mellnik <i>et al.</i> ¹⁸	Bi ₂ Se ₃ /Py	ST-FMR	$\xi_S=2.0-3.5$ $\xi_A \approx 2.5$	$\sigma_S=110-200$ $\sigma_A \approx 150$	thickness and device dependent
Han <i>et al.</i> ⁶¹	Bi ₂ Se ₃ /CoTb (Bi,Sb) ₂ Te ₃ /CoTb	Hysteresis shift	$\xi_S=0.16$ $\xi_S=0.40$	$\sigma_S=15$ $\sigma_S=10$	
Wang <i>et al.</i> ⁵⁷	Bi ₂ Se ₃ /CoFeB	ST-FMR	0.3-1.6		thickness dependent
Wang <i>et al.</i> ⁶⁹	Bi ₂ Se ₃ /CoFeB	ST-FMR	$\xi_S=0.047-0.42$ $\xi_A=0-0.33$	$\sigma_S=6.3-93$ $\sigma_A=0-73$	temperature dependent
Mahendra <i>et al.</i> ⁶²	Bi _x Se _{1-x} /CoFeB	SHH ST-FMR	$\xi_S=0.45-18.62$ $\xi_S=1.56-8.67$	$\sigma_S=145$	thickness dependent and poly-crystalline
	Bi _x Se _{1-x} /Ta/CoFeB	SHH ST-FMR	$\xi_S=6$ $\xi_S=1.35$		
	Bi ₂ Se ₃ /CoFeB	SHH	$\xi_S=0.35$	$\sigma_S=32$	
Shao <i>et al.</i> ⁶³	Bi ₂ Te ₃ /CoFeB	SHH	$\xi_S=1.76$	$\sigma_S=147$	
	(BiSb) ₂ Te ₃ /CoFeB	SHH	$\xi_S=8.33$	$\sigma_S=146$	
	(BiSb) ₂ Te ₃ /Mo/CoFeB	SHH	$\xi_S=2.66$	$\sigma_S=106$	
	(BiSb) ₂ Te ₃ /Mo/CoFeB	MOKE	$\xi_S=2.66$	$\sigma_S=106$	
Khang <i>et al.</i> ⁶⁸	Bi _{0.9} Sb _{0.1} /Mn _{0.4} Ga _{0.6}	Coercivity change	$\xi_S=52$	$\sigma_S=13000$	non-van der Waals material

Transition Metal Dichalcogenides

Earlier reviews about spintronics based on 2D materials focus on spin injection, transport and detection,^{15,70} and spin-valley coupling.⁷¹ Recently, Lin *et al.*⁷² reviewed functional spintronic devices and circuits based on 2D materials. Current-induced spin polarization in 2D materials and the associated SOT effects have not been reviewed. Here, we focus on SOTs from TMDs and show how the symmetry arguments align with the experimental observations.

Experimental observations of SOTs from TMDs. 2H-MoS₂ is an intensively studied 2D material. It has a hexagonal lattice structure and a space group of P6₃/mmc with each Mo atom bonded with 6 S atoms, as illustrated by Fig. 4 (a). Monolayer MoS₂ has a space

group of $P6/mmc$ since there is no 3-fold screw symmetry along the c -axis. When interfacing to an FM layer, the structure of the materials fulfills the symmetry requirements to generate the conventional τ_{DL} and τ_{FL} due to the symmetry breaking at the interface. However, neither monolayer nor multilayer MoS_2/FM heterostructures fulfill the symmetry requirements to generate unconventional SOTs, since there is more than one mirror plane perpendicular to an in-plane axis as illustrated by Fig. 4 (a).

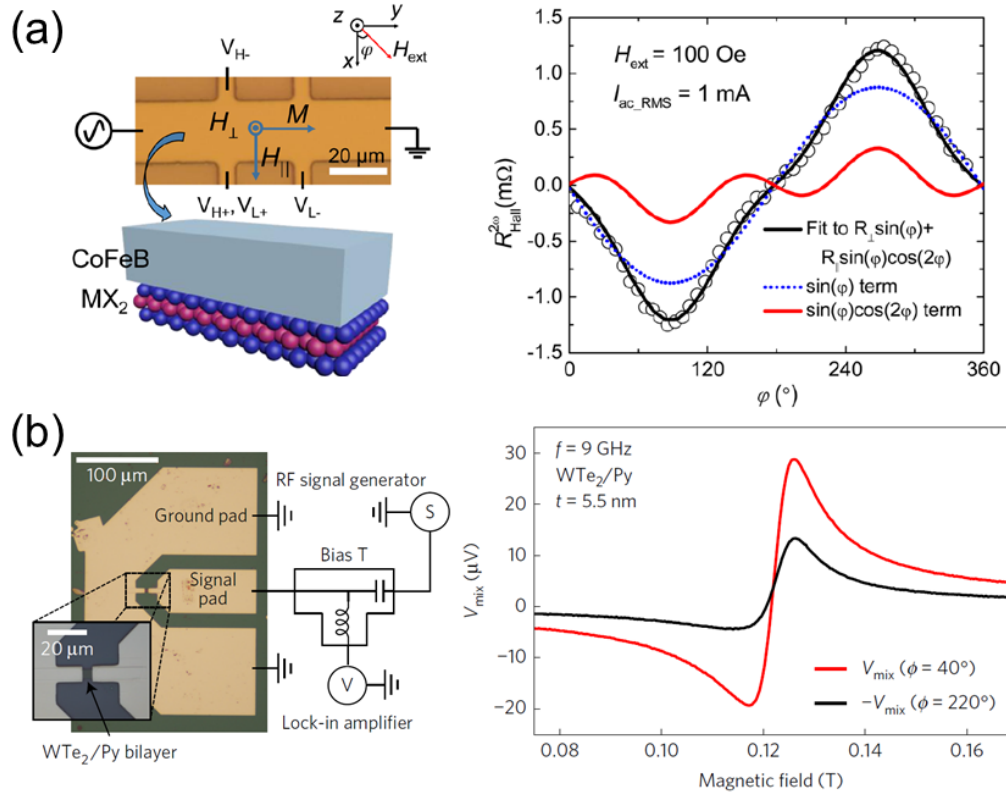


Figure 7: The measurement setup and results of SOTs from TMDs. (a) Measurement setup of SOT measurements for the MX_2/CoFeB heterostructures and the second-harmonic Hall resistance as a function of in-plane azimuthal angle (ϕ) with an external magnetic field 100 Oe applied. (b) The ST-FMR measurement setup on the SOT of WTe_2/Py heterostructures and ST-FMR signals for a $\text{WTe}_2(5.5\ \text{nm})/\text{Py}(6\ \text{nm})$ sample with current applied along the a -axis. ϕ is angle between the current and magnetization. The figures are adapted from Shao *et al.*²² and Macnei *et al.*¹⁰

Shao *et al.*²² reported the SOTs generated by monolayer MoS_2 and WSe_2 with CoFeB at

room temperature, as illustrated in Fig.7 (a), using the SHH method. Different SOTs can be distinguished by analyzing different contributions to the azimuthal angle (φ) dependence of the second harmonic Hall resistance ($R_H^{2\omega}$). As shown in Fig.7 (a), the current is applied along the y-axis and φ is the angle between magnetization and the x-axis. If the magnetization of the FM layer is always in the plane, for an in-plane current, the potentially generated conventional τ_A and unconventional τ_B will be out-of-plane and the conventional τ_S and unconventional τ_T will be in-plane. The in-plane SOTs modulate the anomalous Hall resistance that is independent of φ . The out-of-plane SOTs modulate the planar Hall resistance, contributing to a $\cos(2\varphi)$ dependence. τ_A and τ_S originate from the in-plane spin polarization, contributing to a $\sin\varphi$ dependence. τ_B and τ_T originate from the out-of-plane spin polarization that is independent of φ . In summary, SOT contributions to $R_H^{2\omega}$ can be fitted to the first order using

$$R_H^{2\omega}(\varphi) = A\sin(\varphi)\cos(2\varphi) + B\cos(2\varphi) + S\sin(\varphi) + T,$$

where A , B , S , and T correspond to the contributions from τ_A , τ_B , τ_S , and τ_T , respectively. The typical azimuthal angle dependence of $R_H^{2\omega}(\varphi)$ of MoS₂/CoFeB is shown in Fig.7 (a).²² Only the conventional FL-SOT was observed in this experiment, where σ_A is $2.9 \times 10^3 (\hbar/2e)(\Omega\text{m})^{-1}$ for MoS₂ and $5.5 \times 10^3 (\hbar/2e)(\Omega\text{m})^{-1}$ for WSe₂. Although a $\sin\varphi$ dependence was observed (Fig.7 (a)), it is due to thermoelectric effect instead of SOT effect.²² The observed FL-SOT is attributed to the Rashba-Edelstein effect since it is much larger than the DL-SOT. The generated SOTs can be different if the FM layer is different. Zhang *et al.*²¹ reported the SOTs in a monolayer MoS₂/Py device. The observed symmetric ST-FMR peak is about 4 times bigger than the antisymmetric peak in a MoS₂/Py heterostructure, which suggests that the DL-SOT could be much larger than the FL-SOT according to conventional ST-FMR analysis.⁷³ However, the strength of SOT was not quantified and the origin of SOT was not interpreted due to a potentially large contribution from inverse Rashba-Edelstein

effect-induced spin pumping.

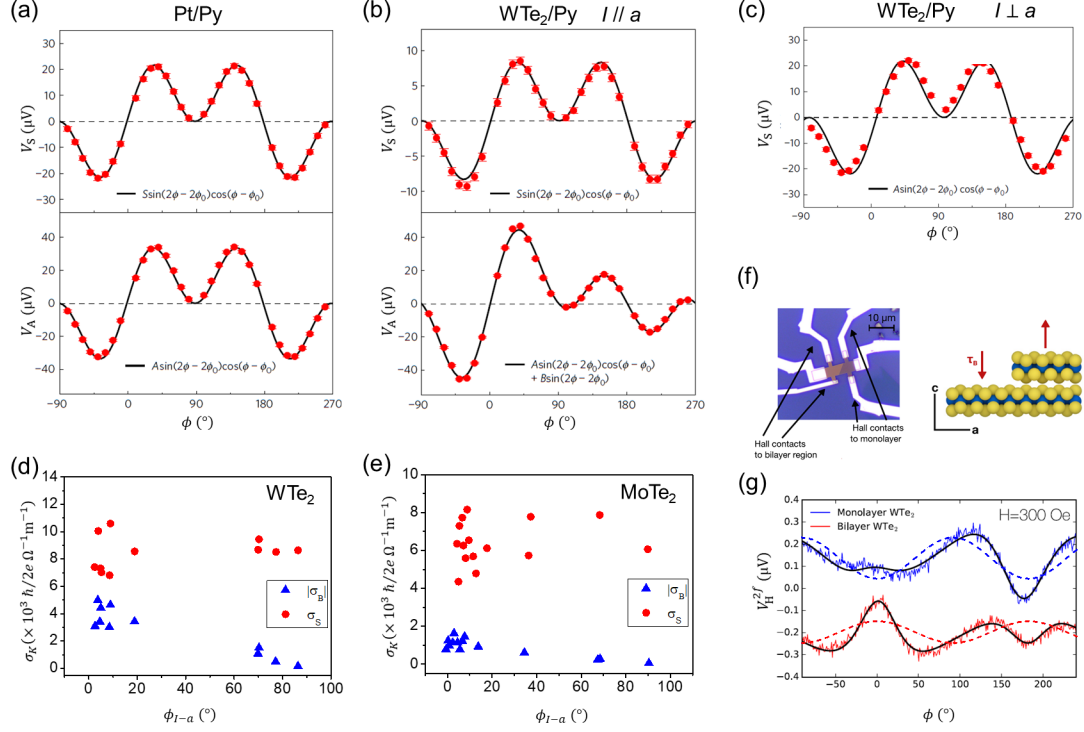


Figure 8: The angular dependence of ST-FMR signals of TMD/Py samples. Azimuthal angle dependence of ST-FMR resonance components for (a) a Pt(6 nm)/Py (6 nm) device, and for a WTe₂(5.5 nm)/Py (6 nm) device with (b) current applied parallel to the *a* axis and (c) current applied perpendicular to the *a* axis. ϕ is the angle between the applied current and magnetization. (d) and (e) τ_B and τ_S as a function of the angle (ϕ_{I-a}) between the applied current and the *a*-axis for WTe₂ and MoTe₂, respectively. (f) The optical micrograph of a WTe₂/Py Hall bar device and schematic of the crystal structure of WTe₂, showing that the surface structure is rotated by 180 degrees across a monolayer step. (g) The second harmonic Hall resistance of the monolayer and bilayer regions. The dash line shows the contribution from the unconventional damping-like SOT. ϕ is the angle between the applied current and magnetization. (a), (b) and (c) are reproduced from MacNeil *et al.*,¹⁰ (d), (f) and (g) are reproduced from MacNeil *et al.*,⁴⁵ (e) is reproduced from Stiehl *et al.*,²⁴

T_d-WTe₂ has a lower crystal symmetry than 2H-MoS₂. It has a primitive lattice which belongs to the C_{2v} point group (space group Pmn2₁). There are a mirror plane perpendicular to its *a* axis, an *n*-glide plane perpendicular to its *b* axis, and a 2-fold screw axis along its *c* axis

as illustrated in Fig. 4 (e). When combined with a ferromagnetic layer such as Py, the 2-fold screw symmetry along c axis and the n -glide symmetry along b axis are broken. This lateral symmetry breaking may lead to the generation of the out-of-plane τ_{DL} , which corresponds to unconventional τ_B . MacNeill *et al.*¹⁰ reported SOTs in a WTe₂/Py heterostructure as shown in Fig. 7 (b). The SOTs were measured by the ST-FMR method. The field dependence of the ST-FMR signal is decomposed into anti-symmetric and symmetric Lorentzian parts (V_A and V_S), which reflect the contributions from out-of-plane and in-plane SOTs, respectively. Since the magnetization of Py is in the plane, τ_A and τ_B will be out-of-plane and τ_S and τ_T will be in-plane. Conventional τ_A and τ_S contributions to the angular dependence of the V_A and V_S can be fitted as a function of $\cos(\varphi)\sin(2\varphi)$ where φ is the angle between magnetization and current (Fig. 8 (a)). Note that the $\cos(\varphi)$ term comes from SOT effects and the $\sin(2\varphi)$ term is from the derivative of anisotropic magnetoresistance since all SOTs modulate it in the ST-FMR signals. Unconventional SOTs originate from an out-of-plane spin polarization that is independent of φ . Therefore, V_B and V_T have a $\sin(2\varphi)$ dependence. In summary, SOT contributions to V_A and V_S can be fitted to the first order using

$$V_A(\varphi) = A\cos(\varphi)\sin(2\varphi) + B\sin(2\varphi)$$

$$V_S(\varphi) = S\cos(\varphi)\sin(2\varphi) + T\sin(2\varphi).$$

In a Pt/Py bilayer, only A and S are observed (see Fig. 8 (a)), which indicates finite τ_A and τ_S . In the case of a WTe₂/Py device, the angular dependence of V_A , as shown by the lower panel of Fig. 8 (b), apparently deviates the $\cos(\varphi)\sin(2\varphi)$ function when the current is applied along a axis. Unconventional τ_B is identified. It is worth noting that the out-of-plane τ_B was not observed when applying current along b as shown in Fig. 8 (c), which agrees well with the symmetry consideration as explained in the previous section. The full angle dependence shows the the current-induced unconventional σ_B reduces when the current gradually changes the direction from the a -axis to the b -axis (Fig. 8 (d)). In contrast, the conventional σ_S does not show a clear change. Similar angle dependence of symmetry breaking-induced

unconventional SOT was also reported in an artificial wedge structure.⁸

The layer dependence of SOT in WTe₂ can be partially explained using the symmetry arguments. The magnitude of out-of-plane DL-SOT (τ_B) shows no significant dependence on the WTe₂ thickness indicating the interfacial nature of τ_B as shown in Fig. 9 (a). However, the sign of the τ_B in the WTe₂/Py can be positive or negative which is in sharp contrast to the fixed sign in the HM/FM.¹⁰ The authors attributed the sign change to the 2-fold screw symmetry of the bulk WTe₂. As shown in Fig. 8 (f), adjacent WTe₂ layers are related by a 180° rotation around the c axis followed by a half-unit cell (one 2D layer) translation along the c axis. Under the 180° rotation, current along the a axis is reversed and the pseudovector τ_B remains unchanged. Therefore, neighboring layers could contribute to an opposite sign of τ_B and the overall $\tau_B=0$. In a WTe₂/Py bilayer, the 2-fold screw symmetry is broken and thus at the interface, finite τ_B can be expected. This argument was later directly proved by their subsequent work⁴⁵ in which SOTs of devices with a monolayer step have been measured by SHH measurements, as illustrated by Fig. 8 (f). The existence of τ_B is evidenced by the $\cos(2\varphi)$ angle dependence in the SHH voltage as shown in Fig. 8 (g). τ_B of two Hall bar regions across a monolayer step have opposite signs. As shown in Fig. 8 (g), the signs of τ_B are opposite for a monolayer and a bilayer WTe₂. In contrast, in all devices without a monolayer step, two Hall bar regions have the same sign. In the WTe₂/Py, τ_A shows a significant dependence on the layer thickness, which is dominated by the current-induced Oersted field.⁴⁵ Similar to τ_B , the thickness independence of τ_S of the WTe₂/Py device also indicates an interfacial origin.^{10,45} Interestingly, at very large thickness, Shi *et al.*⁷⁴ showed the τ_S is much enhanced (see Fig. 9 (b)).

Monoclinic 2D materials also fulfill the symmetry requirement for generating the out-of-plane τ_{DL} despite the fact that monoclinic 2D materials are inversion symmetric by themselves. Stiehl *et al.*²⁴ have investigated the SOTs of the β or 1T' phase MoTe₂. Its lattice structure belongs to the C_{2h} point group (space group: P2₁/m) which has a 2-fold screw

Table 4: The crystal structures and spin conductivities of 2D/FM heterostructures

Authors	Materials	Point group (space group)	Spin conductivity ($\times 10^3 (\hbar/2e)(\Omega m)^{-1}$)	Note
Shao <i>et al.</i> ²²	MoS ₂ /CoFeB	P6/mmc	$\sigma_A = 2.9$	
	WSe ₂ /CoFeB	P6/mmc	$\sigma_A = 5.5$	
MacNeil <i>et al.</i> ¹⁰	WTe ₂ /Py	Pmn2 ₁	$\sigma_A = 9 \pm 3$	thickness independent < 10 nm
			$\sigma_S = 8 \pm 2$	
Shi <i>et al.</i> ⁷⁴	WTe ₂ /Py	Pmn2 ₁	$\sigma_B = 3.68 \pm 0.8$	thickness dependent
			σ_A due to Oersted field	
Stiehl <i>et al.</i> ²⁴	MoTe ₂ /Py	P2 ₁ m	$\sigma_S = 4-60$	thickness dependent
			$\sigma_B = 6$	
			σ_A due to Oersted field	
			$\sigma_T = 0-1.0$	
Guimaraes <i>et al.</i> ⁷⁵	NbSe ₂ /Py	P6 ₃ /mmc	$\sigma_S = 4.7-8.2$	thickness dependent and random σ_T due to uncontrollable strain effect
			$\sigma_B = 0-1.8$	
			$\sigma_T = -2-3.5$	
Xu <i>et al.</i> ²⁶	PtTe ₂ /Py	P $\bar{3}$ m1	20-160	thickness dependent

axis along b axis and a mirror plane perpendicular to it. When interfacing to an FM layer, the out-of-plane τ_{DL} is allowed by symmetry when sending current along the b axis. The SOTs were measured by the ST-FMR technique and the observed SOTs in MoTe₂/Py exactly follow this symmetry consideration. Conventional SOTs and the out-of-plane τ_{DL} are all observed when the applied current is along b axis.²⁴ Similar to WTe₂, current-induced unconventional σ_B reduces when the current gradually changes the direction from the a -axis to the b -axis (Fig. 8 (e)). The layer dependence of σ_B and σ_S reveals an interfacial origin (Fig. 9 (c)).

TaTe₂ has a space group of C2/ m . The layer stacking direction is along its b axis as indicated by Fig. 4 (k). According to its space group notation, there is a 2-fold rotation axis about b axis and a mirror plane perpendicular to it. The surface normal direction deviates from the b axis, hence the 2-fold rotation symmetry is broken. Unconventional SOTs are allowed by symmetry in this material. Stiehl *et al.*²⁵ have studied SOTs in TaTe₂/Py. However, no unconventional SOTs were observed, which could be due to the weak SOC in TaTe₂.²⁵ In the same work, the authors examined the importance of considering the resistance asymmetry of low-symmetry 2D materials in determining the SOTs.

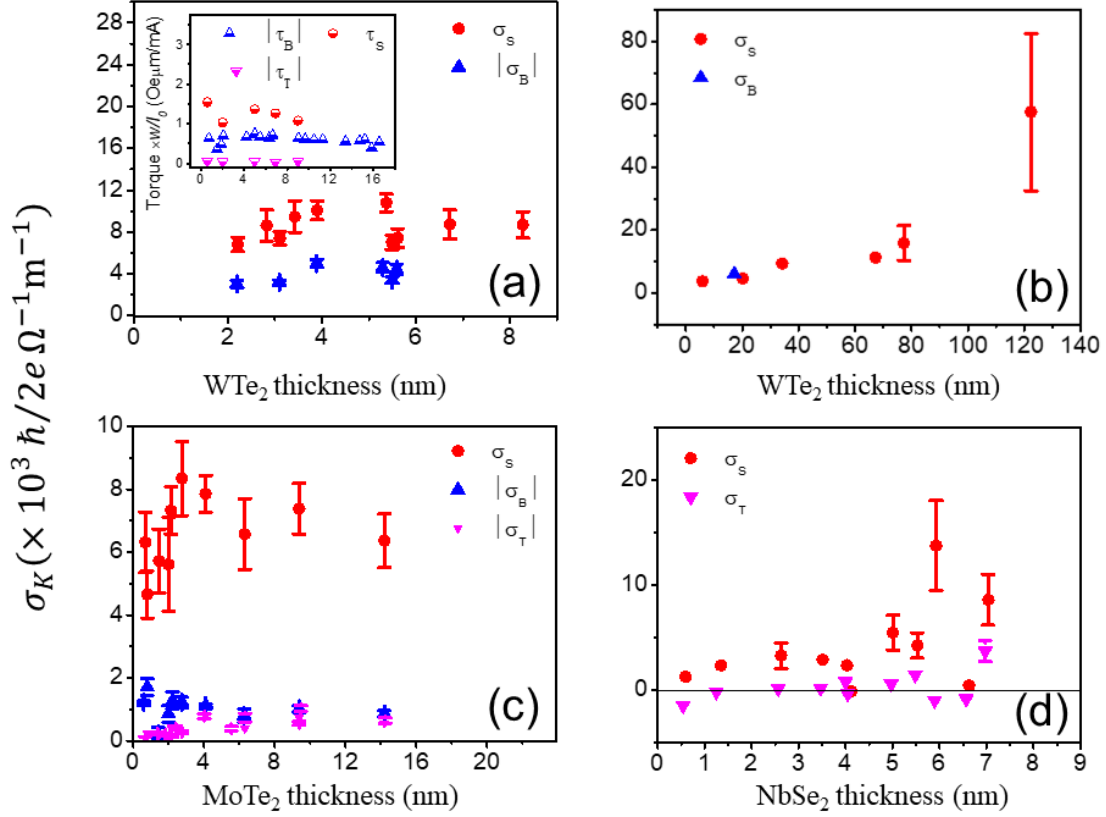


Figure 9: The thickness dependent of SOT or spin conductivities of various TMD/Py devices, where σ_S stands for the conventional damping-like torque, σ_B stands for the out-of-plane damping-like torque and σ_T stands for the out-of-plane field-like torque. The spin conductivities as a function of the thickness of (a) and (b) WTe₂, (c) MoTe₂ and (d) NbSe₂. These figures are reproduced from Macneill *et al.*,^{10,45} Shi *et al.*,⁷⁴ Stiehl *et al.*,²⁴ and Guimaraes *et al.*.²⁷

Some results indicate a possibility to generate the unconventional SOTs in highly symmetric TMDs by using strain effect. Guimaraes *et al.*⁷⁵ have reported SOTs in NbSe₂/Py as shown in Fig. 9 (d). NbSe₂ has a hexagonal structure belonging to a space group of P6₃/mmc which preserves more than one mirror plane perpendicular to an in-plane axis. Like 2H-MoS₂, unconventional SOTs are prohibited by symmetry requirements. However, an unconventional FL-SOT (τ_T) was observed. The magnitude and sign of the (τ_T) don't show any trends with the NbSe₂ thickness and they vary strongly among samples. The authors attributed the arising torque to a strain effect induced by the device fabrication which cannot be controlled at this stage. This strain effect breaks the rotation symmetry and reduces the number of mirror planes to one. As a result, unconventional SOTs are allowed. The crystal structure and spin conductivity of TMDs are summarized in Table 4.

At last, we would like to discuss the origin of the unconventional SOTs. There are two possible mechanisms for the unconventional SOTs. The first one is SHE. This mechanism is recently evidenced by Song *et al.*¹⁶ and Safeer *et al.*¹⁷ that an out-of-plane σ attributing to the intrinsic SHE and inverse SHE has been observed in a few layers MoTe₂ with a non-local spin detection. The second mechanism could attribute to the Rashba effect that originates from the hybridization between the FM layer and the top layers.¹⁰ However, there are still phenomena that cannot be explained using these two models. For example, the layer dependence of τ_B in MoTe₂/Py shows that τ_B is observed in mono- and triple-layered MoTe₂ but not in double-layered MoTe₂²⁴ (Fig. 9 (c)). The exact mechanism for the absence of τ_B in the bilayer MoTe₂ remains unclear.

Growth of 2D Materials for Spintronic Applications

Up to now, most of 2D materials used for SOT studies are not scalable due to the small sample size or difficulty in integration with the CMOS technology. For practical SOT device applications, it is critical to validate three important concepts (see Fig. 10). First, it is

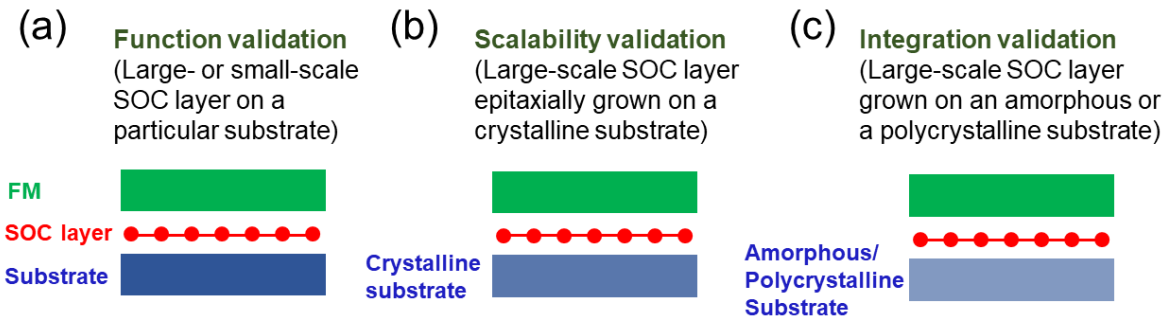


Figure 10: Steps toward practical SOT devices based on crystalline SOC layers, including 2D materials.

function validation, where a 2D material grown on a particular substrate or exfoliated on a substrate is used. As described above, large-scale TIs have been grown using molecular beam epitaxy (MBE) on different substrates⁷⁶ and they have been used to demonstrate a giant SOT efficiency. In contrast, TMDs are exfoliated on a substrate, such as a silicon wafer with thermal oxide, and then FM layers are deposited on them for SOT studies. In this step, two important things need to be validated. First, the SOT magnitudes need to be precisely quantified. Second, the ratio of SOT switching current to the thermal stability factor needs to be assessed. It would be much better if the SOT switching current is determined when the FM layer is in the single domain regime, which is usually achieved by nanopatterning the FM layer into nanodot. So far, most of SOT studies on 2D materials are at this stage. Second, it is scalability validation. While 2D materials prepared by mechanical exfoliation could have exceptional crystalline quality, they are not scalable. There are four commonly used methods to grow crystalline 2D materials: MBE, chemical vapor deposition (CVD), metal-organic CVD (MOCVD), and magnetron sputtering. For a review of the MBE growth of TIs, readers can check Kou *et al.*⁷⁶ For a review of the TMD growth using the first three approaches, readers can check Manzeli *et al.*⁷⁷ Early attempts to deposit high-quality TMD materials using magnetron sputtering have been reported by Huang *et al.*⁷⁸, Samassekou *et al.*⁷⁹ and Wang *et al.*,⁸⁰ where only electrical and optical properties were measured. Re-

cently, Xu *et al.*²⁶ used a two-step process to grow a large-scale PtTe₂ and examined its spintronic properties, revealing a very high σ_S . In the future, spintronic properties of these 2D materials over a large scale need to be systematically quantified. Note that it is critical to ensure single crystallinity and single thickness of the 2D material over the wafer scale. The reason is twofold. First, for TIs, the thickness affects the SOT magnitude significantly⁵⁷ and thus thickness fluctuations may cause variation in switching current. Second, to utilize the out-of-plane damping-like SOT generated by TMDs, random crystalline domains may contribute random out-of-plane FL-SOT directions, which make large-scale production of SOT devices impractical. Therefore, it is necessary to use a single-crystalline substrate (or buffer).

Third, it is integration validation. Eventually, SOT devices need to be integrated with standard CMOS technology using the back-end-of-line (BEOL) process, where the crystalline SOC layer needs to interface an amorphous or polycrystalline substrate such as silicon oxide or metals. Even with a buffer layer, the direct growth of single-crystalline SOC layer could be very challenging on an amorphous or polycrystalline substrate over a large scale. Alternatively, transferring a large-scale crystalline SOC layer could be beneficial. In this approach, one needs to grow a high-quality 2D material on a crystalline material or buffer and then transfer it on to the desired substrate. Readers can check Lin *et al.*⁷² for recent progress.

Conclusion and Outlook

In this review, we have presented the systematic analysis of SOTs based on the symmetry argument and show how this method can be used to predict and analyze the SOTs in 2D materials with various crystal symmetries. We highlight the recent progress of giant SOTs in TI-based heterostructures and unconventional out-of-plane damping-like SOTs in TMD-based heterostructures that could be very beneficial for energy-efficient SOT devices. Based on this review, we suggest the following three important research directions in this field as

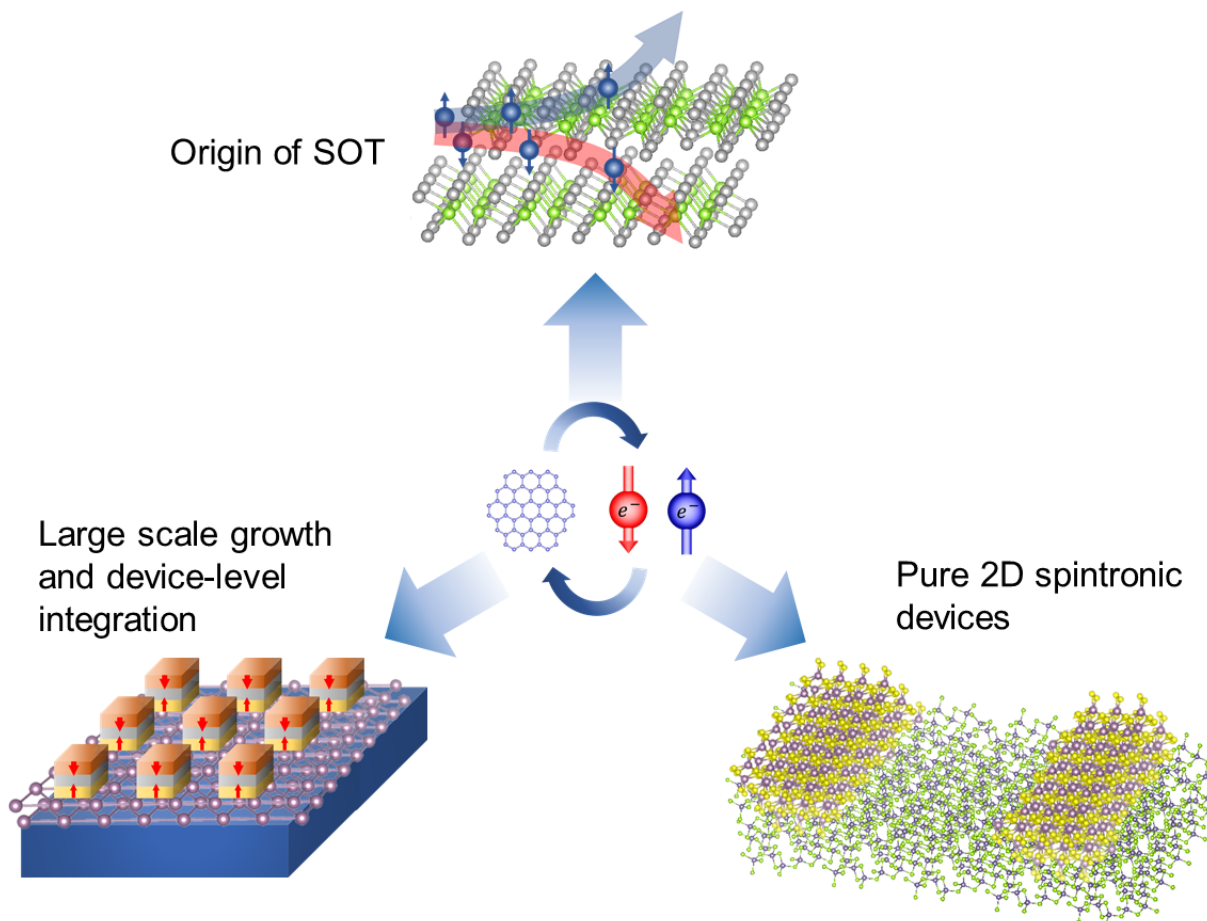


Figure 11: Research directions of 2D material based SOT and spintronic devices.

illustrated in Fig. 11.

(a) understanding the origin of SOTs. While the symmetry argument could provide a qualitative prediction of SOTs, a quantitative prediction relies on the understanding of microscopic picture of SOT generation. Investigating other spin-charge interconversion phenomena such as spin pumping,⁸¹ spin injection,^{16,17} spin thermoelectric effect,⁸² and electrically induced magnetization (magnetoelectricity)⁸³ in 2D material-based heterostructures would also be helpful since they are highly correlated to the SOT physics. 2D materials are layered systems, which are highly anisotropic in crystal structures. The fundamental studies of spin generation and transport in out-of-plane direction are still very limited. As a result, the thickness dependence of SOTs in 2D materials are not well understood.^{24,74}

(b) purely 2D material-based spintronic devices. Recent discoveries of magnetic 2D materials, such as CrI_3 ,¹⁴ $\text{Cr}_2\text{Ge}_2\text{Te}_6$ ¹³ and Fe_3GeTe_2 ,⁸⁴ could enable the integration of non-magnetic 2D materials and magnetic 2D materials for spintronic applications.^{85,86} On the one hand, magnetic 2D materials possess desirable properties for spintronic applications. The excellent gate tunability of magnetic 2D materials allows for exploring magnetoelectric phenomena and applications.⁸⁴ Meanwhile, layered antiferromagnetic 2D materials like CrI_3 exhibit a giant spin-filter tunnel magnetoresistance effect.^{87,88} Furthermore, magnetic ordering of magnetic 2D materials can be manipulated by SOTs.^{89,90} On the other hand, non-magnetic 2D materials could be an excellent spin source owing to their large and multidirectional SOTs as we explained in this review. Besides practical applications, the integration could allow us to explore the exotic phases and interactions in 2D magnetic heterostructures,⁹¹ which are of fundamental interests.

(c) pushing 2D materials towards practical SOT devices. For practical applications, two important factors need to be taken into account. First, 2D materials need to be integrated into CMOS-compatible magnetic materials with PMA.⁶³ Currently, CoFeB/MgO-based MRAM technologies have been mature^{92–94} and it would be very beneficial if 2D materials could be integrated with them. Second, one needs to develop methods of wafer-scale

integration of 2D materials and CMOS-compatible substrates. Potential approaches have been discussed in the large-scale growth section.

Acknowledgement

We thank Wen-Yu He and K. T. Law for insightful discussions. The authors are supported by HKUST ECE start-up fund. The authors use VESTA and *CrystallographyOpenDatabases* for 3D visualizing of crystals.

References

1. Kent, A. D.; Worledge, D. C. A New Spin on Magnetic Memories. *Nature Nanotechnology* **2015**, *10*, 187–191.
2. Sinova, J.; Valenzuela, S. O.; Wunderlich, J.; Back, C. H.; Jungwirth, T. Spin Hall Effects. *Reviews of Modern Physics* **2015**, *87*, 1213–1260.
3. Miron, I. M.; Garello, K.; Gaudin, G.; Zermatten, P.-J.; Costache, M. V.; Auffret, S.; Bandiera, S.; Rodmacq, B.; Schuhl, A.; Gambardella, P. Perpendicular Switching of a Single Ferromagnetic Layer Induced by In-Plane Current Injection. *Nature* **2011**, *476*, 189–193.
4. Liu, L.; Pai, C.-F.; Li, Y.; Tseng, H. W.; Ralph, D. C.; Buhrman, R. A. Spin-Torque Switching with the Giant Spin Hall Effect of Tantalum. *Science* **2012**, *336*, 555–558.
5. Manchon, A.; Železný, J.; Miron, I.; Jungwirth, T.; Sinova, J.; Thiaville, A.; Garello, K.; Gambardella, P. Current-induced Spin-Orbit Torques in Ferromagnetic and Antiferromagnetic Systems. *Reviews of Modern Physics* **2019**, *91*, 035004.
6. Wang, K. L.; Kou, X.; Upadhyaya, P.; Fan, Y.; Shao, Q.; Yu, G.; Amiri, P. K. Electric-

- Field Control of Spin-Orbit Interaction for Low-Power Spintronics. *Proceedings of the IEEE* **2016**, *104*, 1974–2008.
7. Chen, T.; Dumas, R. K.; Eklund, A.; Muduli, P. K.; Houshang, A.; Awad, A. A.; Dürrenfeld, P.; Malm, B. G.; Rusu, A.; Åkerman, J. Spin-Torque and Spin-Hall Nano-Oscillators. *Proceedings of the IEEE* **2016**, *104*, 1919–1945.
 8. Yu, G.; Upadhyaya, P.; Fan, Y.; Alzate, J. G.; Jiang, W.; Wong, K. L.; Takei, S.; Bender, S. A.; Chang, L.-T.; Jiang, Y.; Lang, M.; Tang, J.; Wang, Y.; Tserkovnyak, Y.; Amiri, P. K.; Wang, K. L. Switching of Perpendicular Magnetization by Spin-Orbit Torques in the Absence of External Magnetic Fields. *Nature Nanotechnology* **2014**, *9*, 548–554.
 9. Fan, Y.; Upadhyaya, P.; Kou, X.; Lang, M.; Takei, S.; Wang, Z.; Tang, J.; He, L.; Chang, L.-T.; Montazeri, M.; Yu, G.; Jiang, W.; Nie, T.; Schwartz, R. N.; Tserkovnyak, Y.; Wang, K. L. Magnetization Switching Through Giant Spin-Orbit Torque in a Magnetically Doped Topological Insulator Heterostructure. *Nature Materials* **2014**, *13*, 699–704.
 10. MacNeill, D.; Stiehl, G. M.; Guimaraes, M. H. D.; Buhrman, R. A.; Park, J.; Ralph, D. C. Control of Spin-Orbit Torques Through Crystal Symmetry in WTe₂/Ferromagnet Bilayers. *Nature Physics* **2017**, *13*, 300–305.
 11. Fan, Y.; Kou, X.; Upadhyaya, P.; Shao, Q.; Pan, L.; Lang, M.; Che, X.; Tang, J.; Montazeri, M.; Murata, K.; Chang, L.-T.; Akyol, M.; Yu, G.; Nie, T.; Wong, K. L.; Liu, J.; Wang, Y.; Tserkovnyak, Y.; Wang, K. L. Electric-Field Control of Spin-Orbit Torque in a Magnetically Doped Topological Insulator. *Nature Nanotechnology* **2016**, *11*, 352–359.
 12. Balakrishnan, J.; Kok Wai Koon, G.; Jaiswal, M.; Castro Neto, A. H.; Özyilmaz, B.

- Colossal Enhancement of Spin-Orbit Coupling in Weakly Hydrogenated Graphene. *Nature Physics* **2013**, *9*, 284–287.
13. Gong, C.; Li, L.; Li, Z.; Ji, H.; Stern, A.; Xia, Y.; Cao, T.; Bao, W.; Wang, C.; Wang, Y.; Qiu, Z. Q.; Cava, R. J.; Louie, S. G.; Xia, J.; Zhang, X. Discovery of Intrinsic Ferromagnetism in Two-Dimensional Van Der Waals Crystals. *Nature* **2017**, *546*, 265–269.
 14. Huang, B.; Clark, G.; Navarro-Moratalla, E.; Klein, D. R.; Cheng, R.; Seyler, K. L.; Zhong, D.; Schmidgall, E.; McGuire, M. A.; Cobden, D. H.; Yao, W.; Xiao, D.; Jarillo-Herrero, P.; Xu, X. Layer-Dependent Ferromagnetism in a Van Der Waals Crystal down to the Monolayer Limit. *Nature* **2017**, *546*, 270–273.
 15. Han, W.; Kawakami, R. K.; Gmitra, M.; Fabian, J. Graphene Spintronics. *Nature Nanotechnology* **2014**, *9*, 794–807.
 16. Song, P.; Hsu, C.-H.; Vignale, G.; Zhao, M.; Liu, J.; Deng, Y.; Fu, W.; Liu, Y.; Zhang, Y.; Lin, H.; Pereira, V. M.; Loh, K. P. Coexistence of Large Conventional and Planar Spin Hall Effect with Long Spin Diffusion Length in A Low-Symmetry Semimetal at Room Temperature. *Nature Materials* **2020**, *19*, 292–298.
 17. Safeer, C. K.; Ontoso, N.; Inglá-Aynés, J.; Herling, F.; Pham, V. T.; Kurzmann, A.; Ensslin, K.; Chuvilin, A.; Robredo, I.; Vergniory, M. G.; de Juan, F.; Hueso, L. E.; Calvo, M. R.; Casanova, F. Large Multidirectional Spin-to-Charge Conversion in Low-Symmetry Semimetal MoTe₂ at Room Temperature. *Nano Letters* **2019**, *19*, 8758–8766.
 18. Mellnik, A. R.; Lee, J. S.; Richardella, A.; Grab, J. L.; Mintun, P. J.; Fischer, M. H.; Vaezi, A.; Manchon, A.; Kim, E.-A.; Samarth, N.; Ralph, D. C. Spin-Transfer Torque Generated by a Topological Insulator. *Nature* **2014**, *511*, 449–451.
 19. Soluyanov, A. A.; Gresch, D.; Wang, Z.; Wu, Q.; Troyer, M.; Dai, X.; Bernevig, B. A. Type-II Weyl Semimetals. *Nature* **2015**, *527*, 495–498.

20. Qian, X.; Liu, J.; Fu, L.; Li, J. Quantum Spin Hall Effect in Two-Dimensional Transition Metal Dichalcogenides. *Science* **2014**, *346*, 1344–1347.
21. Zhang, W.; Sklenar, J.; Hsu, B.; Jiang, W.; Jungfleisch, M. B.; Xiao, J.; Fradin, F. Y.; Liu, Y.; Pearson, J. E.; Ketterson, J. B.; Yang, Z.; Hoffmann, A. Research Update: Spin Transfer Torques in Permalloy on Monolayer MoS₂. *APL Materials* **2016**, *4*, 032302.
22. Shao, Q.; Yu, G.; Lan, Y.-W.; Shi, Y.; Li, M.-Y.; Zheng, C.; Zhu, X.; Li, L.-J.; Amiri, P. K.; Wang, K. L. Strong Rashba-Edelstein Effect-Induced Spin-Orbit Torques in Monolayer Transition Metal Dichalcogenide/Ferromagnet Bilayers. *Nano Letters* **2016**, *16*, 7514–7520.
23. Li, P.; Wu, W.; Wen, Y.; Zhang, C.; Zhang, J.; Zhang, S.; Yu, Z.; Yang, S. A.; Manchon, A.; Zhang, X.-X. Spin-Momentum Locking and Spin-Orbit Torques in Magnetic Nano-Heterojunctions Composed of Weyl Semimetal WTe₂. *Nature Communications* **2018**, *9*, 1–10.
24. Stiehl, G. M.; Li, R.; Gupta, V.; Baggari, I. E.; Jiang, S.; Xie, H.; Kourkoutis, L. F.; Mak, K. F.; Shan, J.; Buhrman, R. A.; Ralph, D. C. Layer-Dependent Spin-Orbit Torques Generated by the Centrosymmetric Transition Metal Dichalcogenide Beta-MoTe₂. *Physical Review B* **2019**, *100*, 184402.
25. Stiehl, G. M.; MacNeill, D.; Sivadas, N.; El Baggari, I.; Guimarães, M. H. D.; Reynolds, N. D.; Kourkoutis, L. F.; Fennie, C. J.; Buhrman, R. A.; Ralph, D. C. Current-Induced Torques with Dresselhaus Symmetry Due to Resistance Anisotropy in 2D Materials. *ACS Nano* **2019**, *13*, 2599–2605.
26. Xu, H.; Wei, J.; Zhou, H.; Feng, J.; Xu, T.; Du, H.; He, C.; Huang, Y.; Zhang, J.; Liu, Y.; Wu, H.-C.; Guo, C.; Wang, X.; Guang, Y.; Wei, H.; Peng, Y.; Jiang, W.; Yu, G.; Han, X. High Spin Hall Conductivity in Large-Area Type-II Dirac Semimetal PtTe₂. *Advanced Materials* **2020**, *32*, 2000513.

27. Guimarães, M.; Koopmans, B. Spin Accumulation and Dynamics in Inversion-Symmetric van der Waals Crystals. *Physical Review Letters* **2018**, *120*, 266801.
28. Slonczewski, J. C. Current-Driven Excitation of Magnetic Multilayers. *Journal of Magnetism and Magnetic Materials* **1996**, *159*, L1–L7.
29. Berger, L. Emission of Spin Waves by a Magnetic Multilayer Traversed by A Current. *Physical Review B* **1996**, *54*, 9353–9358.
30. Katine, J. A.; Albert, F. J.; Buhrman, R. A.; Myers, E. B.; Ralph, D. C. Current-Driven Magnetization Reversal and Spin-Wave Excitations in Co /Cu /Co Pillars. *Physical Review Letters* **2000**, *84*, 3149–3152.
31. Myers, E. B.; Ralph, D. C.; Katine, J. A.; Louie, R. N.; Buhrman, R. A. Current-Induced Switching of Domains in Magnetic Multilayer Devices. *Science* **1999**, *285*, 867–870.
32. Yu, G. Two-Terminal MRAM with a Spin. *Nature Electronics* **2018**, *1*, 496–497.
33. Manchon, A.; Zhang, S. Theory of Nonequilibrium Intrinsic Spin Torque in a Single Nanomagnet. *Physical Review B* **2008**, *78*, 212405.
34. Manchon, A.; Zhang, S. Theory of Spin Torque Due to Spin-Orbit Coupling. *Physical Review B* **2009**, *79*, 094422.
35. Chernyshov, A.; Overby, M.; Liu, X.; Furdyna, J. K.; Lyanda-Geller, Y.; Rokhinson, L. P. Evidence for Reversible Control of Magnetization in a Ferromagnetic Material by Means of Spin-Orbit Magnetic Field. *Nature Physics* **2009**, *5*, 656–659.
36. Wang, K. L.; Alzate, J. G.; Amiri, P. K. Low-Power Non-Volatile Spintronic Memory: STT-RAM and Beyond. *Journal of Physics D: Applied Physics* **2013**, *46*, 074003.
37. Lee, K.-S.; Lee, S.-W.; Min, B.-C.; Lee, K.-J. Threshold Current for Switching of a Perpendicular Magnetic Layer Induced by Spin Hall Effect. *Applied Physics Letters* **2013**, *102*, 112410.

38. Liu, L.; Lee, O. J.; Gudmundsen, T. J.; Ralph, D. C.; Buhrman, R. A. Current-Induced Switching of Perpendicularly Magnetized Magnetic Layers Using Spin Torque from the Spin Hall Effect. *Physical Review Letters* **2012**, *109*.
39. Manchon, A.; Koo, H. C.; Nitta, J.; Frolov, S. M.; Duine, R. A. New Perspectives for Rashba Spin–Orbit Coupling. *Nature Materials* **2015**, *14*, 871–882.
40. He, W.-Y.; Law, K. T. Novel Magnetoelectric Effects in Gyrotropic Superconductors. *Physical Review Research* **2020**, *2*, 012073.
41. Symmetry@Otterbein - Symmetry Resources at Otterbein University. <https://symotter.org/>.
42. Character Tables for Chemically Important Point Groups. <http://symmetry.jacobs-university.de/>.
43. Seemann, M.; Ködderitzsch, D.; Wimmer, S.; Ebert, H. Symmetry-Imposed Shape of Linear Response Tensors. *Physical Review B* **2015**, *92*, 155138.
44. Wimmer, S.; Seemann, M.; Chadova, K.; Ködderitzsch, D.; Ebert, H. Spin-Orbit-Induced Longitudinal Spin-polarized Currents in Nonmagnetic Solids. *Physical Review B* **2015**, *92*, 041101.
45. MacNeill, D.; Stiehl, G. M.; Guimarães, M. H. D.; Reynolds, N. D.; Buhrman, R. A.; Ralph, D. C. Thickness Dependence of Spin-Orbit Torques Generated by WTe₂. *Physical Review B* **2017**, *96*, 054450.
46. Li, L.; Han, W.; Pi, L.; Niu, P.; Han, J.; Wang, C.; Su, B.; Li, H.; Xiong, J.; Bando, Y.; Zhai, T. Emerging in-Plane Anisotropic Two-Dimensional Materials. *InfoMat* **2019**, *1*, 54–73.
47. Zhao, S.; Dong, B.; Wang, H.; Wang, H.; Zhang, Y.; Han, Z. V.; Zhang, H. In-plane

- Anisotropic Electronics Based on Low-Symmetry 2D Materials: Progress and Prospects. *Nanoscale Advances* **2020**, *2*, 109–139.
48. Saito, R.; Tatsumi, Y.; Huang, S.; Ling, X.; Dresselhaus, M. S. Raman Spectroscopy of Transition Metal Dichalcogenides. *Journal of Physics: Condensed Matter* **2016**, *28*, 353002.
49. Zhang, H.; Liu, C.-X.; Qi, X.-L.; Dai, X.; Fang, Z.; Zhang, S.-C. Topological Insulators in Bi_2Se_3 , Bi_2Te_3 and Sb_2Te_3 with a Single Dirac Cone on the Surface. *Nature Physics* **2009**, *5*, 438–442.
50. Brown, B. E. The Crystal Structures of NbTe_2 and TaTe_2 . *Acta Crystallographica* **1966**, *20*, 264–267.
51. Huang, H.; Zhou, S.; Duan, W. Type-II Dirac Fermions in the PtSe_2 Class of Transition Metal Dichalcogenides. *Physical Review B* **2016**, *94*, 121117.
52. Weng, H.; Dai, X.; Fang, Z. Transition-Metal Pentatelluride ZrTe_5 and HfTe_5 : a Paradigm for Large-Gap Quantum Spin Hall Insulators. *Physical Review X* **2014**, *4*, 011002.
53. Pesin, D.; MacDonald, A. H. Spintronics and Pseudospintronics in Graphene and Topological Insulators. *Nature Materials* **2012**, *11*, 409–416.
54. Fan, Y.; Wang, K. L. Spintronics Based on Topological Insulators. *SPIN* **2016**, *06*, 1640001.
55. Wang, Y.; Ramaswamy, R.; Yang, H. FMR-Related Phenomena in Spintronic Devices. *Journal of Physics D: Applied Physics* **2018**, *51*, 273002.
56. Wu, H.; Zhang, P.; Deng, P.; Lan, Q.; Pan, Q.; Razavi, S.; Che, X.; Huang, L.; Dai, B.; Wong, K.; Han, X.; Wang, K. Room-Temperature Spin-Orbit Torque from Topological Surface States. *Physical Review Letters* **2019**, *123*, 207205.

57. Wang, Y.; Zhu, D.; Wu, Y.; Yang, Y.; Yu, J.; Ramaswamy, R.; Mishra, R.; Shi, S.; Elyasi, M.; Teo, K.-L.; Wu, Y.; Yang, H. Room Temperature Magnetization Switching in Topological Insulator-Ferromagnet Heterostructures by Spin-Orbit Torques. *Nature Communications* **2017**, *8*, 1–6.
58. Che, X.; Pan, Q.; Vareskic, B.; Zou, J.; Pan, L.; Zhang, P.; Yin, G.; Wu, H.; Shao, Q.; Deng, P.; Wang, K. L. Strongly Surface State Carrier-Dependent Spin–Orbit Torque in Magnetic Topological Insulators. *Advanced Materials* **2020**, *32*, 1907661.
59. Kondou, K.; Yoshimi, R.; Tsukazaki, A.; Fukuma, Y.; Matsuno, J.; Takahashi, K. S.; Kawasaki, M.; Tokura, Y.; Otani, Y. Fermi-level-Dependent Charge-to-Spin Current Conversion by Dirac Surface States of Topological Insulators. *Nature Physics* **2016**, *12*, 1027–1031.
60. Wang, Y.; Deorani, P.; Qiu, X.; Kwon, J. H.; Yang, H. Determination of Intrinsic Spin Hall Angle in Pt. *Applied Physics Letters* **2014**, *105*, 152412.
61. Han, J.; Richardella, A.; Siddiqui, S. A.; Finley, J.; Samarth, N.; Liu, L. Room-Temperature Spin-Orbit Torque Switching Induced by a Topological Insulator. *Physical Review Letters* **2017**, *119*, 077702.
62. De, M.; Grassi, R.; Chen, J.-Y.; Jamali, M.; Hickey, D. R.; Zhang, D.; Zhao, Z.; Li, H.; Quarterman, P.; Lv, Y.; Li, M.; Manchon, A.; Mkhoyan, K. A.; Low, T.; Wang, J.-P. Room-Temperature High Spin-Orbit Torque Due to Quantum Confinement in Sputtered $\text{Bi}_x\text{Se}_{1-x}$ Films. *Nature Materials* **2018**, *17*, 800–807.
63. Shao, Q.; Wu, H.; Pan, Q.; Zhang, P.; Pan, L.; Wong, K.; Che, X.; Wang, K. L. Room Temperature Highly Efficient Topological Insulator/Mo/CoFeB Spin-Orbit Torque Memory with Perpendicular Magnetic Anisotropy. 2018 IEEE International Electron Devices Meeting (IEDM). 2018; pp 36.3.1–36.3.4.

64. You, L.; Lee, O.; Bhowmik, D.; Labanowski, D.; Hong, J.; Bokor, J.; Salahuddin, S. Switching of Perpendicularly Polarized Nanomagnets with Spin Orbit Torque Without an External Magnetic Field by Engineering a Tilted Anisotropy. *Proceedings of the National Academy of Sciences* **2015**, *112*, 10310–10315.
65. Fukami, S.; Zhang, C.; DuttaGupta, S.; Kurenkov, A.; Ohno, H. Magnetization Switching by Spin–Orbit Torque in an Antiferromagnet–Ferromagnet Bilayer System. **2016**, *15*, 535–541.
66. Oh, Y.-W.; Chris Baek, S.-h.; Kim, Y. M.; Lee, H. Y.; Lee, K.-D.; Yang, C.-G.; Park, E.-S.; Lee, K.-S.; Kim, K.-W.; Go, G.; Jeong, J.-R.; Min, B.-C.; Lee, H.-W.; Lee, K.-J.; Park, B.-G. Field-free Switching of Perpendicular Magnetization Through Spin–Orbit Torque in Antiferromagnet/Ferromagnet/Oxide Structures. *Nature Nanotechnology* **2016**, *11*, 878–884.
67. Li, X.; Lin, S.-J.; DC, M.; Liao, Y.-C.; Yao, C.; Naeemi, A.; Tsai, W.; Wang, S. X. Materials Requirements of High-Speed and Low-Power Spin-Orbit-Torque Magnetic Random-Access Memory. *IEEE Journal of the Electron Devices Society* **2020**, 1–1.
68. Khang, N. H. D.; Ueda, Y.; Hai, P. N. A Conductive Topological Insulator with Large Spin Hall Effect for Ultralow Power Spin-Orbit Torque Switching. *Nature Materials* **2018**, *17*, 808–813.
69. Wang, Y.; Deorani, P.; Banerjee, K.; Koirala, N.; Brahlek, M.; Oh, S.; Yang, H. Topological Surface States Originated Spin-Orbit Torques in Bi₂Se₃. *Physical Review Letters* **2015**, *114*, 257202.
70. Han, W. Perspectives for Spintronics in 2D Materials. *APL Materials* **2016**, *4*, 032401.
71. Schaibley, J. R.; Yu, H.; Clark, G.; Rivera, P.; Ross, J. S.; Seyler, K. L.; Yao, W.; Xu, X. Valleytronics in 2D Materials. *Nature Reviews Materials* **2016**, *1*, 1–15.

72. Lin, X.; Yang, W.; Wang, K. L.; Zhao, W. Two-Dimensional Spintronics for Low-Power Electronics. *Nature Electronics* **2019**, *2*, 274–283.
73. Liu, L.; Moriyama, T.; Ralph, D. C.; Buhrman, R. A. Spin-Torque Ferromagnetic Resonance Induced by the Spin Hall Effect. *Physical Review Letters* **2011**, *106*, 036601.
74. Shi, S.; Liang, S.; Zhu, Z.; Cai, K.; Pollard, S. D.; Wang, Y.; Wang, J.; Wang, Q.; He, P.; Yu, J.; Eda, G.; Liang, G.; Yang, H. All-Electric Magnetization Switching and Dzyaloshinskii-Moriya Interaction in WTe₂/Ferromagnet Heterostructures. *Nature Nanotechnology* **2019**, *14*, 945–949.
75. Guimarães, M. H. D.; Stiehl, G. M.; MacNeill, D.; Reynolds, N. D.; Ralph, D. C. Spin-Orbit Torques in NbSe₂/Permalloy Bilayers. *Nano Letters* **2018**, *18*, 1311–1316.
76. Kou, X.; Wang, K. L. *Bismuth-Containing Alloys and Nanostructures*; Springer Series in Materials Science; Springer, Singapore, 2019; Vol. 285; pp 319–349.
77. Manzeli, S.; Ovchinnikov, D.; Pasquier, D.; Yazyev, O. V.; Kis, A. 2D Transition Metal Dichalcogenides. *Nature Reviews Materials* **2017**, *2*.
78. Huang, J.-H.; Deng, K.-Y.; Liu, P.-S.; Wu, C.-T.; Chou, C.-T.; Chang, W.-H.; Lee, Y.-J.; Hou, T.-H. Large-Area 2D Layered MoTe₂ by Physical Vapor Deposition and Solid-Phase Crystallization in a Tellurium-Free Atmosphere. *Advanced Materials Interfaces* **2017**, *4*, 1700157.
79. Samassekou, H.; Alkabsh, A.; Wasala, M.; Eaton, M.; Walber, A.; Walker, A.; Pitkänen, O.; Kordas, K.; Talapatra, S.; Jayasekera, T.; Mazumdar, D. Viable Route Towards Large-Area 2D MoS₂ Using Magnetron Sputtering. *2D Materials* **2017**, *4*, 021002.
80. Wang, J.; Jiang, Z.; Chen, H.; Li, J.; Yin, J.; Wang, J.; He, T.; Yan, P.; Ruan, S. High Energy Soliton Pulse Generation by A Magnetron-Sputtering-Deposition-Grown MoTe₂ Saturable Absorber. *Photonics Research* **2018**, *6*, 535.

81. Mendes, J. B. S.; Aparecido-Ferreira, A.; Holanda, J.; Azevedo, A.; Rezende, S. M. Efficient Spin to Charge Current Conversion in the 2D Semiconductor MoS₂ by Spin Pumping from Yttrium Iron Garnet. *Applied Physics Letters* **2018**, *112*, 242407.
82. Dau, M. T.; Vergnaud, C.; Marty, A.; Beigné, C.; Gambarelli, S.; Maurel, V.; Journot, T.; Hyot, B.; Guillet, T.; Grévin, B.; Okuno, H.; Jamet, M. The Valley Nernst Effect in WSe₂. *Nature Communications* **2019**, *10*, 5796.
83. Lee, J.; Wang, Z.; Xie, H.; Mak, K. F.; Shan, J. Valley Magnetoelectricity in Single-Layer MoS₂. *Nature Materials* **2017**, *16*, 887–891.
84. Deng, Y.; Yu, Y.; Song, Y.; Zhang, J.; Wang, N. Z.; Sun, Z.; Yi, Y.; Wu, Y. Z.; Wu, S.; Zhu, J.; Wang, J.; Chen, X. H.; Zhang, Y. Gate-Tunable Room-Temperature Ferromagnetism in Two-Dimensional Fe₃GeTe₂. *Nature* **2018**, *563*, 94–99.
85. Gong, C.; Zhang, X. Two-Dimensional Magnetic Crystals and Emergent Heterostructure Devices. *Science* **2019**, *363*.
86. Zhang, W.; Wong, P. K. J.; Zhu, R.; Wee, A. T. S. Van Der Waals Magnets: Wonder Building Blocks for Two-Dimensional Spintronics? *InfoMat* **2019**, *1*, 479–495.
87. Song, T.; Cai, X.; Tu, M. W.-Y.; Zhang, X.; Huang, B.; Wilson, N. P.; Seyler, K. L.; Zhu, L.; Taniguchi, T.; Watanabe, K.; McGuire, M. A.; Cobden, D. H.; Xiao, D.; Yao, W.; Xu, X. Giant Tunneling Magnetoresistance in Spin-Filter Van Der Waals Heterostructures. *Science* **2018**, *360*, 1214–1218.
88. Klein, D. R.; MacNeill, D.; Lado, J. L.; Soriano, D.; Navarro-Moratalla, E.; Watanabe, K.; Taniguchi, T.; Manni, S.; Canfield, P.; Fernández-Rossier, J.; Jarillo-Herrero, P. Probing Magnetism in 2D Van Der Waals Crystalline Insulators via Electron Tunneling. *Science* **2018**, *360*, 1218–1222.

89. Alghamdi, M.; Lohmann, M.; Li, J.; Jothi, P. R.; Shao, Q.; Aldosary, M.; Su, T.; Fokwa, B. P. T.; Shi, J. Highly Efficient Spin-Orbit Torque and Switching of Layered Ferromagnet Fe_3GeTe_2 . *Nano Letters* **2019**, *19*, 4400–4405.
90. Wang, X.; Tang, J.; Xia, X.; He, C.; Zhang, J.; Liu, Y.; Wan, C.; Fang, C.; Guo, C.; Yang, W.; Guang, Y.; Zhang, X.; Xu, H.; Wei, J.; Liao, M.; Lu, X.; Feng, J.; Li, X.; Peng, Y.; Wei, H. *et al.* Current-Driven Magnetization Switching in a Van Der Waals Ferromagnet Fe_3GeTe_2 . *Science Advances* **2019**, *5*, eaaw8904.
91. Zhao, W.; Fei, Z.; Song, T.; Choi, H. K.; Palomaki, T.; Sun, B.; Malinowski, P.; McGuire, M. A.; Chu, J.-H.; Xu, X.; Cobden, D. H. Magnetic Proximity and Nonreciprocal Current Switching in a Monolayer WTe_2 Helical Edge. *Nature Materials* **2020**, *19*, 503–507.
92. Garello, K.; Yasin, F.; Couet, S.; Souriau, L.; Swerts, J.; Rao, S.; Van Beek, S.; Kim, W.; Liu, E.; Kundu, S.; Tsvetanova, D.; Croes, K.; Jossart, N.; Grimaldi, E.; Baumgartner, M.; Crotti, D.; Fumémont, A.; Gambardella, P.; Kar, G. SOT-MRAM 300MM Integration for Low Power and Ultrafast Embedded Memories. 2018 IEEE Symposium on VLSI Circuits. 2018; pp 81–82.
93. Golonzka, O.; Alzate, J. G.; Arslan, U.; Bohr, M.; Bai, P.; Brockman, J.; Buford, B.; Connor, C.; Das, N.; Doyle, B.; Ghani, T.; Hamzaoglu, F.; Heil, P.; Hentges, P.; Jahan, R.; Kencke, D.; Lin, B.; Lu, M.; Mainuddin, M.; Meterelliyoz, M. *et al.* MRAM as Embedded Non-Volatile Memory Solution for 22FFL FinFET Technology. 2018 IEEE International Electron Devices Meeting (IEDM). 2018; pp 18.1.1–18.1.4.
94. Song, Y. J.; Lee, J. H.; Han, S. H.; Shin, H. C.; Lee, K. H.; Suh, K.; Jeong, D. E.; Koh, G. H.; Oh, S. C.; Park, J. H.; Park, S. O.; Bae, B. J.; Kwon, O. I.; Hwang, K. H.; Seo, B.; Lee, Y.; Hwang, S. H.; Lee, D. S.; Ji, Y.; Park, K. *et al.* Demonstration of

Highly Manufacturable STT-MRAM Embedded in 28nm Logic. 2018 IEEE International Electron Devices Meeting (IEDM). 2018; pp 18.2.1–18.2.4.